ARL-TR-9520 • AUG 2022

Toward Material Property Extraction from Dynamic Spherical Indentation Experiments

by John D Clayton, Daniel T Casem, Jeffrey T Lloyd, and Emily H Retzlaff

NOTICES

Disclaimers

ARL-TR-9520 ● AUG 2022

Toward Material Property Extraction from Dynamic Spherical Indentation Experiments

John D Clayton, Daniel T Casem, and Jeffrey T Lloyd
DEVCOM Army Research Laboratory

Emily H Retzlaff
United States Naval Academy

REPORT DOCUMENTATION PAGE

Form Approved
OMB No. 0704-0188

1. REPORT DATE *(DD-MM-YYYY)*
August 2022

2. REPORT TYPE
Technical Report

3. DATES COVERED (From - To)
January 2022–August 2022

4. TITLE AND SUBTITLE
Toward Material Property Extraction from Dynamic Spherical Indentation Experiments

5a. CONTRACT NUMBER

5b. GRANT NUMBER

5c. PROGRAM ELEMENT NUMBER

6. AUTHOR(S)
John D Clayton, Daniel T Casem, Jeffrey T Lloyd, and Emily H Retzlaff

5d. PROJECT NUMBER

5e. TASK NUMBER

5f. WORK UNIT NUMBER

7. PERFORMING ORGANIZATION NAME(S) AND ADDRESS(ES)
DEVCOM Army Research Laboratory
ATTN: FCDD-RLW-TB
Aberdeen Proving Ground, MD 21005-5066

8. PERFORMING ORGANIZATION REPORT NUMBER
ARL-TR-9520

9. SPONSORING/MONITORING AGENCY NAME(S) AND ADDRESS(ES)

10. SPONSOR/MONITOR'S ACRONYM(S)

11. SPONSOR/MONITOR'S REPORT NUMBER(S)

12. DISTRIBUTION/AVAILABILITY STATEMENT
Approved for public release; distribution is unlimited.

13. SUPPLEMENTARY NOTES
primary author's email: <john.d.clayton1.civ@army.mil>.

14. ABSTRACT

A new treatment of dynamic indentation using dimensional analysis is forwarded, and a general framework for extraction of material property information (i.e., constitutive model parameters) from spherical indentation experiments is set forth. Static indentation is reviewed as a prerequisite to dynamic indentation, since the former is a subset of the latter with inertia, rate dependence, and adiabatic heating removed. Experimental data obtained from instrumented spherical indentation in a miniature Kolsky bar apparatus are evaluated via the proposed method of dimensional analysis. The substrate material is aluminum alloy Al6061-T6. Several definitions of indentation strain proposed for static indentation are newly assessed for dynamic indentation, as are indentation strain rates. The analysis suggests that while fidelity of the experimental method and inertial effects could inhibit extraction of elastic properties, extraction of certain plastic constitutive properties is feasible. However, current data are insufficient to enable determination of a complete and unique set of all physical properties. Motivated by the current results, new experiments and simulations are proposed that would enable identification of influential properties, facilitating inverse analysis.

15. SUBJECT TERMS
indentation, metals, plasticity, rate dependence, constitutive modeling

16. SECURITY CLASSIFICATION OF:			**17. LIMITATION OF ABSTRACT**	**18. NUMBER OF PAGES**	**19a. NAME OF RESPONSIBLE PERSON**
a. REPORT	**b. ABSTRACT**	**c. THIS PAGE**			John D Clayton
Unclassified	Unclassified	Unclassified	UU	53	**19b. TELEPHONE NUMBER (Include area code)** 410-278-6146

Standard Form 298 (Rev. 8/98)
Prescribed by ANSI Std. Z39.18

Contents

List of Figures

List of Tables

Acknowledgments

The authors acknowledge support from the intramural component of the High-Throughput Materials Discovery for Extreme Conditions program at the US Army Combat Capabilities Development Command (DEVCOM) Army Research Laboratory (ARL). Information exchanges with Prof Surya Kalidindi of the Georgia Institute of Technology on spherical indentation experiments and models are acknowledged as well.

1. Introduction

Indentation experiments, being relatively simple and inexpensive to perform, offer the possibility of high-throughput mechanical testing, i.e., numerous experiments conducted in rapid time. Other advantages include the following: only small samples of material are needed, and response variations in different regions of heterogeneous bodies can be easily probed.[1] Furthermore, numerical simulations of spherical indentation of elastic-plastic solids are now routinely accomplished using conventional finite element (FE) methods with widely available commercial software.[2–4] The disadvantage of the indentation experiment, relative to traditional mechanical testing (e.g., uniaxial tension/compression), is proper analysis of the resulting data.[5] Stress and strain fields are highly nonuniform during indentation. Friction at the interface, pile-up, and sink-in effects complicate analysis.[2,3,6] In dynamic indentation, strain rate is also highly nonuniform, even if the indenter velocity is constant. Inevitably, the indenter will decelerate prior to unloading, drastically reducing the average strain rate over time.

The present research is focused on issues associated with extraction of material constitutive properties from dynamic spherical indentation tests. The discussion is geared toward ductile elastic-plastic solids (e.g., engineering metals), though some issues are shared among other material classes. Materials with viscoelastic response,[7,8] or those undergoing brittle fracture,[9] are not addressed explicitly.

Governing relationships among global variables are cast in dimensionless form in a new application of dimensional analysis to dynamic spherical indentation. Relationships among useful dependent and independent variables are analyzed in the context of Buckingham's Pi theorem.[7,10,11] This approach, which enables a systematic reduction of the number of independent quantities entering a physical problem, has been used previously to analyze static spherical indentation[12] and ballistic impact.[13] Here, the treatment of Lee and Komvopoulos[14] is extended to account for thermal effects, and different mathematically admissible (and thought more physically useful) choices are made for independent and dependent variables of interest. Results provide guidance on which parameter(s) should be varied systematically in a design of experiments, real or numerical, to enable a complete understanding of the problem. Outcomes are then applied to experimental data on an aluminum alloy, producing dimensionless indentation force, contact area, and global temperature rise. Different indentation strains and strain rates are calculated and examined for potential suitability in the context of constitutive model determination.

This report is organized as follows. Pertinent aspects of static indentation, notably governing equations and constitutive model forms, are reviewed first in Section 2, since many carry over to the dynamic regime. Dynamic indentation is addressed in Section 3, including extension of constitutive models to incorporate rate and temperature, as well as several proposed definitions of effective indentation strain rate. Dimensional analysis of dynamic spherical indentation is undertaken in Section 4. Techniques are applied to newly acquired, instrumented indentation data for aluminum alloy Al6061-T6 in Section 5. Recommendations are given for future experiments, and possible numerical simulations, that would facilitate constitutive model parameterization using dynamic spherical indentation data. Lastly, conclusions follow in Section 6.

2. Static Indentation

The scientific literature on static indentation, even when focused purely on modeling techniques for material property extraction, is immense. A thorough review of the subject is thus outside the present scope, which instead reports details needed in subsequent dimensional analysis of the dynamic case. See the book by Johnson[15] for seminal analytical methods applied to contact problems, and two review papers[5,16] for contemporary overviews that include computer simulations.

2.1 Elastic Indentation

The linear isotropic elastic solutions of Hertz are conventionally used to analyze static indentation data up to initial yield, as well as elastic unloading from a plastically deformed state. The Hertz analysis[15] assumes frictionless contact of homogeneous elastic bodies whose surfaces are parabolic in shape. In the limit of small indentation depths and contact areas pertinent to the elastic regime, the quadratic surface approximation adequately represents the true spherical geometry of the indenter.[17] Provided that the yield strength of the material is a small fraction of the elastic stiffness, effects of elastic nonlinearity are typically deemed negligible, and thus omitted in nearly all reported analytical and numerical studies of indentation of ductile metals. However, for large *elastic* indentation depths, nonlinear compressibility has been shown to mildly increase indentation force.[18]

Hertz's equations for spherical indentation into an initially flat substrate are summarized as follows.[1,15] Denote by P the indentation force, h_e the elastic (i.e., reversible) indentation depth, $\bar{E}$ the effective system modulus, $\bar{R}$ the effective system radius, a the contact radius, and $\bar{k}$ a system stiffness. Denote by $E_i, E_s, \nu_i, \nu_s, R_i, R_s$ the elastic moduli, Poisson's ratios, and radii of the indenter and sample, labeled with respective subscripts $(\cdot)_i$ and $(\cdot)_s$. Then Hertz's solution encompasses

$$P = \bar{k} h_e^{3/2}, \qquad \bar{k} = \tfrac{4}{3} \bar{E} \bar{R}^{1/2}, \qquad a = (\bar{R} h_e)^{1/2}; \tag{1}$$

$$\bar{E} = [(1 - \nu_i^2)/E_i + (1 - \nu_s^2)/E_s)]^{-1}, \qquad \bar{R} = (1/R_i + 1/R_s)^{-1}. \tag{2}$$

For a rigid indenter, $\bar{E} = E_s$ and $R_i =$ constant, and prior to deformation $R_s \to \infty \Rightarrow \bar{R} = R_i$. If the indenter is deformable, a typical approximation for its elastic displacement h_i is given by Hertz's solution for indentation into a rigid flat surface[1]:

$$h_i \approx 3(1 - \nu_i^2) P / (4 E_i a). \tag{3}$$

The effective system modulus $\bar{E}$ encompasses all effects of material constitutive behavior on the load-displacement curves in the linear elastic regime. This modulus has also been widely used to fully encompass *elastic* constitutive effects on load-displacement response in the elastic-plastic regime, e.g., in dimensional analysis.[19–21] Justification for this assumption in early stages of elastic-plastic indentation has been obtained from analytical methods[15,22] and verified for $\nu_s \in [0.01, 0.49]$ in FE simulations.[3] For a very stiff or rigid indenter, effects of Poisson's ratio of the sample on indentation force are small relative to effects of elastic modulus of the sample over typical ranges of constitutive behaviors of ductile metals.[7,23,24] In other words, sensitivity of load-displacement to Poisson's ratio is typically low, though exceptions exist for unusual material property combinations[25] and for large indentation depths.[3]

2.2 Elastic-plastic Indentation

In the elastic-plastic regime, the total indentation depth for the system, h, is decomposed into[1]

$$h = h_e + h_r = h_s + h_i; \qquad h_e = (P/\bar{k})^{2/3}. \tag{4}$$

The elastic indentation depth of the system is h_e, and when the indenter deforms only elastically, its indentation displacement h_i can be approximated via Eq. 3. The residual indentation depth is h_r; after elastic unloading, $h = h_r$ and $h_e = h_i = 0$.

During elastic unloading, the slope of the load-indentation curve is the derivative

$$S(h) = \mathrm{d}P(h)/\mathrm{d}h_e = \tfrac{2}{3}\bar{k}(h) \cdot h_e^{1/2} = 2\bar{E} \cdot a(h). \tag{5}$$

If S is measured at a given elastic-plastic contact depth h,[6] then the contact radius a at that depth can be inferred from Eq. 5 if $\bar{E}$ is known.[26]

Constitutive behavior of a ductile metallic specimen is typically described via isotropic elasto-plasticity with possible power-law hardening.[21,27–30] Although subtle differences exist among numerous functional forms of hardening laws given in the literature, a reasonably standard model for von Mises-equivalent flow stress σ is

$$\sigma(\epsilon^P) = \sigma_0 \left[1 + \kappa \cdot (\epsilon^P)^n\right], \qquad m = \mathrm{d}\ln\sigma/\mathrm{d}\ln\epsilon^P. \tag{6}$$

Cumulative scalar plastic strain is ϵ^P, the strain hardening exponent is n, and κ is a fitting parameter. For perfect plasticity, $\kappa = 0$, and for linear hardening, $n = 1$ with $\kappa > 0$.

Standard, physically justified, and established methods (i.e., associative flow, normality, consistency) can be used to implement Eq. 6 in the context of finite deformations with incremental plasticity in a numerical setting[31]:

$$\mathrm{d}\boldsymbol{\epsilon} = \mathrm{d}\boldsymbol{\epsilon}^E + \mathrm{d}\boldsymbol{\epsilon}^P, \qquad \mathrm{d}w^P = \boldsymbol{\sigma} : \mathrm{d}\boldsymbol{\epsilon}^P = \sigma \mathrm{d}\epsilon^P. \tag{7}$$

The tensor-valued strain increment $\mathrm{d}\boldsymbol{\epsilon}$ is additively decomposed into elastic $(\cdot)^E$ and plastic $(\cdot)^P$ parts, the stress tensor is $\boldsymbol{\sigma}$, and the scalar plastic strain increment $\mathrm{d}\epsilon^P$ is obtained from the increment of the plastic strain tensor such that its work conjugate entering plastic work per unit volume w^P is the von Mises stress σ. For uniaxial stress conditions, such treatment reduces to, with ϵ the total axial strain,

$$\sigma = \begin{cases} E\epsilon & (\epsilon \leq \sigma_0/E), \\ \sigma_0\left[1 + \kappa \cdot (\epsilon^P)^n\right] & (\epsilon \geq \sigma_0/E). \end{cases} \tag{8}$$

Define the projected contact area by A, and the mean contact pressure by $\bar{p}$, where the latter is identified with Meyer's hardness H in an indentation hardness experiment (i.e., spherical indentation on a flat substrate for a Brinell test):

$$\bar{p} = \frac{P}{A} = \frac{P}{\pi a^2} = H \approx c\bar{\sigma}. \tag{9}$$

An effective value of the flow stress σ in the sample is $\bar{\sigma}$, and c is the constraint factor that depends on geometry, and to a lesser extent, constitutive behavior.[2,6,32,33] Yielding in the sample is initiated at $c \approx 1.1$,[6,32] whereby h_p first becomes nonzero. For sufficiently deep indentation, $h \gg h_e$ such that the plastic response dominates. In this regime, analysis and data of Tabor[34] suggest $c \approx 2.8$ for spherical indentation in ductile metals, later corroborated by numerical methods by Hill et al.[35] Another typical approximation is $c \approx 3$ for this regime.[6] In an intermediate regime between elastic and deep indentation, $1.1 \lesssim c \lesssim 3$.

For strain hardening materials ($n > 0$), c likely depends on both n and the definition used for "indentation strain" $\bar{\epsilon}$ substituted into Eq. 8 for ϵ^P to acquire a representative value of $\bar{\sigma}$.[2,6] Tabor[34] proposed $\epsilon^P \approx \bar{\epsilon} = 0.2a/R_i$, which corresponds to plastic strain at the indentation edge.[2] In that work,[34] $a \approx a_r$ was approximated as the radius a_r of the residual indent after load removal, and thus is not consistent with the Hertz definition of the true contact area at the instant load removal begins. Additionally, the approximation $R \approx R_i$ is often used in practice rather than the second of Eq. 2 to characterize unloading from a plastically deformed state, an approximation which tends to poorly capture the effective stress-strain behavior and unloading modulus.[5]

A potential difficulty with many definitions for indentation strain[6,34] is determination of the contact radius a, which may be challenging to obtain directly from experiments. An estimate proposed by Field and Swain[6] for this purpose is

$$a = [2(h - h_e/2)R_i - (h - h_e/2)^2]^{1/2}. \tag{10}$$

However, noted by Kalidindi and Pathak[17] is that the definition of a in Eq. 10, based on spherical geometry assuming elastic displacement of a preformed spherical impression is evenly divided above and below the circle of contact,[6] is not fully consistent with Hertz's definition in Eq. 1.

An alternative measure of indentation strain $\hat{\epsilon}$, with corresponding stress $\hat{\sigma}$, is thus proposed by Kalidindi and Pathak[5,17]:

$$\hat{\epsilon} = \frac{4}{3\pi}\frac{h_s}{a} \approx \frac{h_s}{2.4a}, \qquad \hat{\sigma} = \bar{p} = \frac{P}{\pi a^2} \approx c\bar{\sigma}. \tag{11}$$

The contact radius incorporated in these works[5,17] obeys the Hertz definition in Eq. 1 and can be found from Eq. 5 during unloading, provided $\bar{E}$ is known from fitting to data collected in the elastic regime. Note that Eq. 11 produces $\hat{\sigma} = \bar{E}\hat{\epsilon}$ for $h = h_e$, i.e., for elastic loading/unloading commensurate with the Hertz solution Eq. 1. Application of Eq. 11 to experimental[1] and numerical[27,28] results produces a constraint factor of $c \approx 2$ for metals with no strain hardening, or for strain-hardening metals at a uniaxial-equivalent offset strain of $\epsilon \approx 0.1\% - 0.2\%$. Possible reasons for $c < 2.8$ in some investigations[1,27,28] are shallower indentation depths than used by Tabor and others[2,34,35] and different definitions or measures of a among the different investigations.

Three indentation strain measures are collected below for reference and comparison:

- Tabor[34]: $\bar{\epsilon} = 0.2 \cdot (a/R_i)$;
- Kalidindi and Pathak[17]: $\hat{\epsilon} = (4/\{3\pi\}) \cdot (h_s/a)$;
- Lee and Komvopoulos[36]: $\check{\epsilon} = (E_s/\sigma_0) \cdot (h/\{2R_i h - h^2\}^{1/2})$.

Notably, constitutive scaling factor E_s/σ_0 is present in $\check{\epsilon}$, while the other two measures are purely geometric. Only $\hat{\epsilon}$ requires knowledge of two transient variables (i.e., a and h_s).

2.3 Constitutive Property Extraction

Numerous works have sought to extract uniaxial stress-strain constitutive behavior from spherical indentation data in the quasi-static regime, claiming various degrees of success. A relatively simple model for loading-unloading cycles[6] incorporating Eq. 10 is widely mentioned, though it is not valid for the transition regime $1.1 \lesssim c \lesssim 3$. Early FE simulations[35,37,38] of quasi-static spherical indentation date to the 1980s. Existence, uniqueness, and stability of the inverse solution have been investigated in the context of dimensional analysis.[21,25] In related work,[21] a representative strain is determined that renders a dimensionless indentation force independent of strain hardening exponent. An optimal data acquisition location from which to extract field variables from FE solutions for material property evaluation has been proposed.[39] An average representative strain and confidence domain for which property correlations are accurate have been defined.[40,41]

Inverse methods incorporating numerically generated databases of spherical indentation response data have been used for property extraction.[30,42,43] More sophisticated data-driven approaches utilize neural networks[29,44,45] or Bayesian inference.[28,46] Simplified analytical fitting functions or surrogate numerical models (i.e., calibrated replacements of full FE models) can be invoked in this context to greatly improve computational efficiency.[28,29] Though not of present focus, spherical indentation FE simulations have also been used to understand anisotropic elastic and plastic properties.[47,48]

Most often, correlation of the loading portion of a predicted force-displacement curve with test data[2] is used to determine plasticity parameters (e.g., σ_0, κ, n), while unloading is used to determine elastic stiffness $\bar{E}$ with some estimate of the contact area.[6] However, periodic load-unload cycles can be used to determine the projected contact area $A = \pi a^2$ if $\bar{E}$ is measured from the initial elastic loading phase.[17] The strategy advocated by Kalidindi and coworkers[5,27,28] involves fitting or comparison of indentation stress-strain curves rather than indentation force-displacement curves to ascertain elastic-plastic properties. Elastic-plastic properties have been identified by numerically matching residual imprints,[42,46] as opposed to force-displacement curves.

Protocols for generating uniaxial stress-strain curves from indentation stress-strain curves, where the latter follow Eq. 11, are described by Patel and Kalidindi.[27] The equivalent uniaxial stress-strain behavior is of the standard form $\sigma = E_s \cdot \epsilon^E = E_s \cdot (\epsilon - \epsilon^P)$. Then the following relations apply among indentation stress-strain curves ($\hat{\sigma}$ vs. $\hat{\epsilon}$) and uniaxial curves (σ vs. ϵ):

$$\hat{\sigma} = \begin{cases} \bar{E} \cdot \hat{\epsilon} & (\hat{\sigma} \leq c\sigma_0), \\ \bar{E} \cdot (\hat{\epsilon} - \hat{\epsilon}^P) & (\hat{\sigma} > c\sigma_0); \end{cases} \qquad \hat{\epsilon} = \frac{4}{3\pi} \frac{h_s}{a} = \hat{\epsilon}^E + \hat{\epsilon}^P; \tag{12}$$

$$\epsilon^E = \frac{1}{c} \frac{E_s}{\bar{E}} \cdot \hat{\epsilon}^E = \frac{1}{c} \frac{E_s}{\bar{E}} \cdot \frac{\hat{\sigma}}{\bar{E}} = \frac{1}{c} \frac{E_s}{\bar{E}^2} \frac{P}{\pi a^2}, \qquad \epsilon^P = \frac{\hat{\epsilon} - \hat{\epsilon}^E}{\hat{\beta}}. \tag{13}$$

The constraint factor c is measured at the yield point ($\bar{\sigma} = \sigma_0$) for continuity, and $\hat{\beta}$ is a fitting factor that depends on the material. FE simulations for a representative elastic-perfectly plastic solid[27] produce $c \approx 2.2$ and $\hat{\beta} \approx 1.3$. The indentation stress-strain fitting method can be advantageous to fitting of force-displacement responses since pertinent elastic-plastic properties may be strongly correlated to only relatively small regions of the force-displacement curve. Thus, a certain precision of fitting for entire force-displacement curves does not necessarily carry over to similar precision in extracted stress-strain curves, elastic modulus, yield strength, and/or strain hardening parameters.[29] Another method of reducing fitting errors associated with estimation of contact area involves correlation of total and recoverable strain energies (i.e., integrals of load-displacement relations) rather than indentation forces,[7,12] since integral values are less sensitive to experimental noise.

According to Cao and Lu,[21] an inverse problem is ill-posed if one of the following properties is not respected:

- Existence: there exists a solution to the problem.
- Uniqueness: there is, at most, one solution to the problem.
- Stability: the solution continuously depends on the data.

The condition number of an inverse problem measures sensitivity of the identified parameter to small changes in the input data. A problem is ill-conditioned if the condition number is large, and it is ill-posed if the condition number is infinity. A thorough numerical analysis of spherical elasto-plastic indentation[21] found stability to degrade with increasing n and with increasing σ_0/E_s. To the above three criteria, an obvious measure of success of an inverse analysis procedure can be added:

- Accuracy: how closely the inverse solution matches the exact solution.

The exact solution would be procured from independent property specifications or measurements (e.g., uniaxial stress-strain experiments) in the present application to indentation analysis.

Some challenges mentioned in the literature for static property extraction are now reiterated. In Zhao et al.,[23] the error of reverse analysis was less than 10% in most cases, where discrepancies were caused in part by accuracy of fitting functions, and in part by the error of applying a power-law hardening model to real materials. In works by Moussa et al.,[40,41] it was found that extraction of stress-strain curves from indentation gives precise results only over a range of strain, which was termed a "confidence domain". Patel and Kalidindi[27] noted the difficulty with pinpointing an initial yield stress σ_0 when yielding occurs at low indentation depths, given typical resolution of experimental data in this regime. Shallow indentation may not provide sufficient information for discriminating hardening parameters.[28] An opinion stated by Dean and Clyne[43] is that a single indentation run with a spherical indenter should be sufficient for property determination, at least for typical quasi-static isothermal behaviors of ductile metals.

For indenters with self-similar shapes (e.g., conical, Berkovich or Vickers pyramidal), no inherent length scale is introduced by the geometry. It follows that hardness, representative strain, and curvature of the load-displacement relation are independent of indentation depth, which can be proven using dimensional analysis.[7,49,50] This contributes to nonuniqueness of property extraction from a single indentation using such an indenter shape. So-called "mystical materials" exist that have different elastic-plastic property combinations but identical indentation curves obtained from self-similar indenters.[51,52] Nonuniqueness can be rectified by using combined data from indenters of different shapes, e.g., different tip apex angles[20,43,53] to determine material properties from an inverse analysis. In contrast, nonuniqueness is less problematic for spherical indentation since the indenter radius introduces a geometric length scale independent of the indentation depth.[7,12,43]

According to Liu et al.,[52] fundamental plastic constitutive properties such as the yield stress and work hardening coefficient cannot always be uniquely determined from the force-displacement curves of indentation analyses, including both plural sharp indentation and deep spherical indentation. Mystical material pairs can still exist in such cases, with a difference of their force-displacement curves below the resolution of existing indentation techniques for large ranges of sharp indenter angles or spherical indentation depths. From the indentation force-displacement curve alone, it is generally not possible to precisely specify what plastic hardening model should be used (e.g., Eq. 6 vs. some other constitutive equation) for an arbitrary material, and the whole stress-strain curve of the material cannot be measured due to geometric limitations on maximum depth that bound the indentation strain.[52] A Monte Carlo sensitivity analysis[24] demonstrated, in the case of spherical indentation, that the experimental errors must be very small to enable reliable extraction of material properties.

In summary, the existence, uniqueness, stability, and accuracy of an inverse technique for property extraction from static spherical indentation depend on multiple factors. These factors may include the indentation depth and indenter radius, the assumed constitutive model, and presumptive initial conditions (i.e., initial guesses) and bounds on material parameters in a search algorithm. The aforementioned four aspects of performance appear to generally improve as indentation depth increases to the plasticity-dominated regime, wherein the plastic zone under the indenter has enlarged sufficiently to control stiffness of the substrate that is registered at the contact surface. Incorporation of more data in any calibration procedure, including residual indentation geometry and a range of indentation load-unload depths and geometries, is expected to improve results. Fitting of indentation stress-strain data and consideration of energy-displacement data rather than explicit force-displacement data have been observed to improve stability and accuracy. Of course, when the assumed constitutive form is close to true material behavior, with property ranges typical of those for which the constitutive model is intended, success is more likely. On the other hand, for exotic materials (i.e., different from typical ductile metals), or for those with highly uncertain behaviors, success of constitutive model parameterization is not ensured a priori and thus should be verified on a case-by-case basis. For example, if the material exhibits simultaneous viscoelastic and plastic mechanisms, a unique constitutive model prescription from usual indentation data may be impossible.[54]

3. Dynamic Indentation

Substantial research has been directed toward material constitutive characterization using dynamic indentation methods, albeit far less than that for the static regime reviewed in Section 2. Early work[55] analyzed projectile impact of hard spheres into softer metallic targets of much larger dimensions than the spheres. Dynamic stress-strain curves were extracted from analysis of the results. The flow stress was defined as $\bar{p}/c$ with a static value of $c \approx 3$ depending on material, and Tabor's strain measure $\bar{\epsilon} = 0.2a_r/R_i$ was used, with a_r the residual contact radius. More recent experiments[56–58] likewise analyzed hardness data extracted from spherical projectile impact. The above studies are not considered instrumented methods. Rather, these methods rely on knowledge only of the impactor size and initial velocity, and postmortem analysis of the impact crater, to infer material response information, since transient forces and velocities are not recorded in-situ during the event.

Dynamic indentation using the split Hopkinson pressure bar (SHPB) has been implemented for a variety of indenter geometries and target materials, as pioneered by Subhash and co-workers.[59,60] This technique allows for interrogation of velocities and mechanical forces during the transient indentation process. More recent approaches of dynamic indentation with the SHPB have used a full sphere sandwiched between two specimens[61] or a striker with variable impedance to achieve load cycling.[62] Strain rate sensitivity of metals was deduced from dynamic conical indentation experiments by Lu et al.,[63] where the indenter was propelled by a light gas gun, and a combination of interferometry and load transducer was used to ascertain a time-resolved material response including rate sensitivity. Force and velocity histories were recorded from spherical indentation at moderate impact velocities in an instrumented drop-weight system,[64] again to assess rate sensitivity of flow stress.

Dynamic impact experiments with laser-driven flyers[65] may offer an alternative or supplementary means of high-throughput characterization of mechanical properties, at potentially much higher local strain rates and different stress states (e.g., incurring spall) than dynamic indentation with the SHPB. Analysis of such contemporary techniques is outside the scope of this report.

3.1 Dynamic Elastic-plastic Indentation

Analytical and numerical models, the latter primarily dynamic FE methods, have likewise been used to study dynamic indentation, and often more specifically, extract material property information. In addition to mechanisms pertinent to static loading (i.e., elasticity, yield, and strain hardening), wave propagation enters the dynamic problem, necessitating involvement of mass density ρ_0. For high loading rates, conditions are nearly adiabatic and temperature rise could be substantial, so specific heat capacity (e.g., c_V) also affects the response. Finally, dislocation kinetic processes depend on loading rate to varying degrees depending on specific metal. It is assumed that impact conditions are not severe enough to warrant inclusion of nonlinear elasticity (e.g., pressure-dependent compressibility) or thermoelastic coupling (i.e., thermal expansion), which would be needed for accurate analysis of intense shock waves, for example.

Focusing attention again on isotropic ductile polycrystalline metals, the inelastic constitutive model for dynamic loading is usually augmented to account for strain rate and temperature effects, in addition to initial yield and strain hardening. The flow stress of Eq. 6 is often extended as a product of terms accounting for each mechanism, for example,

$$\sigma(\epsilon^P, \dot{\epsilon}^P, T) = \sigma_0 \left[1 + \kappa \cdot (\epsilon^P)^n\right] \cdot f(\dot{\epsilon}^P) \cdot g(T), \tag{14}$$

where T is absolute temperature and $\dot{\epsilon}^P$ is a scalar effective strain rate.[31] Functions f and g account, respectively, for strain rate and thermal sensitivity. A widely used form* is the Johnson-Cook model[66,67]:

$$f = 1 + C \cdot \ln[\dot{\epsilon}^P/\dot{\epsilon}_0], \qquad g = 1 - [(T - T_R)/(T_M - T_R)]^q. \tag{15}$$

In the first of Eq. 15, C is a fitting parameter and $\dot{\epsilon}_0$ is a normalization constant. In the second of Eq. 15, T_R and T_M are a reference temperature and melt temperature, with q a thermal softening exponent. Other models include power-law forms[4,14,63,68]:

$$f = 1 + (\dot{\epsilon}^P/\dot{\epsilon}_0)^m, \qquad g = (T/T_R)^r. \tag{16}$$

In Eq. 16, conventional definitions[69] for material constants are $m = \partial \ln \sigma / \partial \ln \dot{\epsilon}^P$ for strain rate sensitivity and $r = \partial \ln \sigma / \partial \ln T$ for thermal sensitivity. Usually, $C > 0$, $m > 0$, $q > 0$, and $r < 0$, such that strength increases with increasing strain rate and decreasing temperature. In the context of these two models, the number of inelastic constitutive parameters is increased by at least two from the static case, from three (σ_0, κ, n) to five $(\sigma_0, \kappa, n, C$ or m, q or $r)$ if T_R and $\dot{\epsilon}_0$ are interpreted as fixed universal constants. More parameters are necessary to incorporate strain-rate-history effects, and measurements are presumably needed for mass density and specific heat, where the latter two properties do not directly influence solutions to the static indentation problem.

The local temperature rate can be obtained from the continuum balance of energy[69]:

$$\rho_0 c_V \dot{T} \approx \zeta \cdot \dot{w}^P \approx \zeta \cdot \sigma \dot{\epsilon}^P. \tag{17}$$

Thermoelastic coupling is omitted, and adiabatic conditions pertinent to rapid load-

---

*Often in the literature, $\sigma_0 \to A$, $\sigma_0 \cdot \kappa \to B$, and $q \to m$ are used for Johnson-Cook constants.

ing are assumed. The Taylor-Quinney factor is $\zeta \in [0,1]$, typically much closer to unity than zero and assumed constant in practice, though its value is expected to evolve with deformation.[4] Later, the approximation $\zeta = 1$ is used, presuming the missing thermoelastic heating in Eq. 17 is offset by a maximally high value of ζ.

3.2 Prior Work

Important findings from previous modeling of dynamic indentation are summarized next. The analytical model of Mok and Duffy[55] was used to extract dynamic stress-strain curves from sphere-impact experimental data, and a representative strain rate of $\dot{\epsilon} \approx 1500$/s was deduced to match dynamic uniaxial compression stress-strain data. More recently, analytical models have been used to assess dynamic hardness and dynamic rate sensitivity (n) for conical[63] and spherical[70] impacts. An analytical model[56] is used to infer that adiabatic plastic strain localization causes a reduction in hardness for sufficiently high sphere impact velocities, at correspondingly high indentation strains and strain rates.[57,58] The model of Tirupataiah and Sundararjan[56] is used to analyze dynamic sphere impact by Kumaraswamy and Rao,[71] wherein the plastic zone depths from dynamic and static indentation were of similar depth when normalized by indenter diameter. Therein, it is also determined that inertial effects on indentation response were unimportant due to the short time required for stress waves to traverse the contact area, relative to the total duration of the impact event.

An analytical expanding cavity model is derived by Ito and Arai[67] for dynamic spherical impact, showing reasonable correlation of local field variables with those from FE solutions. This analytical model is later invoked[72] to determine strain rate sensitivity parameter C of the Johnson-Cook model from knowledge of indentation craters from spherical impacts obtained from experiments at two or more distinct impact velocities.

FE simulations provide more information than approximate analytical solutions, and thus enable more reliable material response parameter extraction. In Lu et al.,[63] FE simulations with strain rate dependence as in Eq. 16 (but no thermal effects: $g = 1$) are used to validate the strain rate sensitivity extracted from dynamic conical indentation experiments on copper. In Calle et al.,[64] FE simulations are used in conjunction with drop-test data to determine strain rate sensitivity in terms of increase over static yield strength, without direct prescription of a strain-rate-hardening function f as entering Eq. 14. Results are comparable to conventional SHPB rate sensitivity data, thereby validating the method for the particular metals of study: steel, copper, brass, and a titanium alloy.

The residual indentation imprint from dynamic FE simulations of spherical indentation has been used to identify elastic-plastic constitutive parameters,[42] for materials without rate or temperature dependence, i.e., a model of the form in Eq. 6. Similarly, static yield and strain hardening parameters are identified from simulated SHPB-driven dynamic indentation using two conical indenters of different apex angles.[73] Spherical impact data for rate-insensitive, linear hardening materials are generated in dynamic FE simulations[74] for a range of depths and indenter sizes. Then support vector machine algorithms, Gaussian process regression, and nonlinear regressions as machine learning techniques are employed to estimate the material's plastic properties given only certain indentation response data.

Thorough parametric studies of dynamic spherical indentation using FEM have been reported[36] for rate-insensitive elastic-plastic solids ($m = 0$) and were extended[14] for potentially rate-sensitive elastic-plastic solids ($m \geq 0$). In these studies, the indenter is a rigid sphere moving at constant velocity v_i, conditions that differ from experimental protocols wherein velocity usually decreases with depth, and wave speeds of an elastic indenter are finite. Temperature effects are also omitted ($g = 0$), and non-reflecting boundary conditions are invoked such that wave interactions with sample boundaries vanish in the simulations. For impact speeds that are large, mean contact pressure $\bar{\sigma} = P/(\pi a^2)$ is found to significantly exceed $3\sigma_0$ at early simulation times, when inertial effects dominate.

In Lee and Komvopoulos,[14] four possible stages of the dynamic deformation process are identified for spherical indentation at constant rates:

- Elastic-plastic deformation characterized by an elastic core separating the plastic zone from the contact interface;
- Initial surface plastic deformation encountered upon disappearance of the elastic core and occurrence of maximum local plastic strain in the subsurface;
- Transient fully plastic deformation, where maximum local plastic strain shifts close to the contact interface and $c = \bar{\sigma}/\sigma_0$ increases with indentation depth;

- Steady full plastic deformation wherein $c \approx 3$ representing static material hardness. This state is achieved for rate-insensitive materials at sufficient depths, when inertial effects become negligible.

Lee and Komvopoulos[14] discover a dimensionless parameter $\chi = (E_s/\sigma_0)(\upsilon_i/C_l) = [(\frac{1}{2}\rho_0\upsilon_i^2)/(\frac{1}{2}E_s\epsilon_0^2)]^{1/2} = \sqrt{U_k/U_0}$ that is found to delineate elastic-plastic, initial surface plastic, and transient fully plastic regimes achieved in the initial state, respectively, with increasing χ. Here, $C_l = \sqrt{E_s/\rho_0}$ is the longitudinal wave speed for uniaxial stress, U_k is a kinetic energy density, and U_0 is elastic energy density at initial yield strain $\epsilon_0 = \sigma_0/E_s$. For the case of rate-sensitive solids ($m > 0$), mean contact pressure decreases, contact area increases, and plastic work increases with increasing m and increasing static hardening coefficient n. Effects of plastic parameters are more easily delineated when inertial effects decay, as indentation depth and simulation time increase.

3.3 Indentation Strain Rate

When correlating dynamic indentation data with dynamic experimental data that have been recorded at a less fluctuating rate (e.g., recorded from traditional SHPB experiments), a measure of global or effective strain rate for the indentation experiment is often sought. Just as there is no unique definition of global strain for static indentation, no unique definition of indentation strain rate exists. Plastic strain is locally heterogeneous during indentation, and local plastic strain rates are even more so, due to inherent changes in velocity of the indenter (e.g., deceleration after impact) as well as stress wave transients.

Several pragmatic definitions have been proposed elsewhere, in order to assign an effective strain rate to a dynamic hardness H or strength $\bar{\sigma}$ measurement. In Lu et al.,[63] with t_r the loading duration, the following function is proposed for dynamic conical indentation by an indenter of mass m_i, cone angle θ, and initial velocity υ_i:

$$\dot{\epsilon}_r = \frac{\epsilon_R}{t_r}; \qquad \epsilon_R = 0.07, \quad t_r = 1.4\left[\frac{9m_i}{4\upsilon_i}\frac{\tan^2\theta}{\pi\sigma_0}\frac{1}{1+\ln\{[E_s/(3\sigma_0)]\tan\theta\}}\right], \tag{18}$$

where ϵ_R is the representative strain from Atkins and Tabor[75] and t_r is obtained from derivations by Johnson.[22] The strain rate in Eq. 18 is an average measure, i.e., a constant for a given experiment.

Perhaps most often used for spherical indentation is the derivative of Tabor's indentation strain:

$$\dot{\bar{\epsilon}}(t) = \frac{\mathrm{d}}{\mathrm{d}t}\left[0.2\frac{a(t)}{R_i}\right]. \tag{19}$$

A definition for the average strain rate $(\cdot)_A$ over the duration of the experiment, similar to that of Lu et al.[63] but now applicable to spherical indentation, was proposed by Kren et al.,[70] which is obtained by dividing Tabor's indentation strain by the measured loading time t_m for which strain increases:

$$(\dot{\bar{\epsilon}})_A = \frac{1}{t_m}\int_0^{t_m}\frac{\mathrm{d}}{\mathrm{d}t}\left[0.2\frac{a(t)}{R_i}\right]\mathrm{d}t = 0.2\frac{a_m}{R_i t_m}. \tag{20}$$

The contact radius at maximum depth is a_m; this could be substituted with the residual contact radius after unloading, a_r, for consistency with Tabor's techniques.

The following expressions are derived for a rigid indenter ($h_s = h$) of potentially transient velocity $\upsilon_i(t) = \dot{h}(t)$, using Tabor's strain measure and geometry of the indented surface[64]:

$$\begin{aligned}\bar{\epsilon}(t) &= 0.2\frac{a(t)}{R_i} \approx 0.4\left[\frac{h(t)}{2R_i}\left(1-\frac{h(t)}{2R_i}\right)\right]^{1/2} \Rightarrow \\ \dot{\bar{\epsilon}}(t) &\approx \frac{0.1\dot{h}(t)}{R_i}\left[1-\frac{h(t)}{R_i}\right]\left[\frac{h(t)}{2R_i}\left(1-\frac{h(t)}{2R_i}\right)\right]^{-1/2}.\end{aligned} \tag{21}$$

In the context of Eq. 10 derived by Field and Swain,[6] it is assumed in the calculation of the contact radius a in Eq. 21 that $h \approx h_r \gg h_e/2$. For an alternative strain rate definition, differentiation of Eq. 11 produces an effective indentation strain rate of

$$\dot{\hat{\epsilon}}(t) = \frac{4}{3\pi a(t)}\left[\dot{h}_s(t) - \frac{\dot{a}(t)}{a(t)}h_s(t)\right]. \tag{22}$$

Uniaxial-equivalent elastic and plastic strain rates could be obtained from differentiation of Eq. 13. Finally, a general order-of-magnitude relation applicable to any indenter type is defined by Subhash[60]:

$$\dot{\epsilon}_h = \upsilon_i/h, \qquad [\dot{\epsilon}_h = \dot{h}/h \text{ for rigid indenter}]. \tag{23}$$

Here υ_i is a representative velocity of the indenter, and depth h could be substituted with another measure of the size of the impression (e.g., residual imprint diagonal or radius). The rigid-indenter version of Eq. 23 is used in the context of creep and viscoelasticity in Cheng and Cheng.[7] For example, Kren et al.[70] use Eq. 23 with υ_i the initial impact velocity and h replaced by the residual (plastic) contact diameter $2a_r$.

4. Dynamic Dimensional Analysis

In the analysis that follows, two major assumptions are invoked regarding the indenter and contact interface. These assumptions reduce the number of independent parameters, simplifying analysis. Firstly, the indenter is assumed rigid. This is a typical assumption in static and dynamic FE simulations (e.g.,[14,28,36]), most valid when $E_i \gg E_s$. Besides reducing $\bar{E} \to E_s, \bar{R} \to R_i, h \to h_s$ in the Hertz theory of Section 2.1, this assumption eliminates effects of wave transmission in the indenter that could affect contact under dynamic indentation.

Secondly, contact is assumed frictionless, the most common assumption in FE simulations of dynamic indentation.[14,36,64,73] As shown in FE simulations of static indentation,[3] contact friction significantly affects the local strain field in the vicinity of the indenter and has a non-negligible effect on the contact radius versus indentation depth relation. Most calculations show that the load-displacement curve is not significantly affected by friction for static spherical indentation,[3,23,43] though exceptions exist.[21] The assumption of frictionless contact is often made for convenience, but appears in many cases to produce sound agreement between force-depth data extracted from models and experiments.[6,28] In some numerical studies, nonzero (constant) friction coefficients ranging from 0.1 to 0.25 are used,[24,30,42] choices which also seem to enable close agreement with experimental data. Effects of friction for dynamic indentation remain to be elucidated in numerical or experimental studies. The validity of the frictionless assumption likely improves as the surface roughness of sample and indenter decrease.

Several assumptions are also made regarding the testing apparatus. It is assumed that the radius of the indenter $R = R_i$ is variable from experiment to experiment, but that other aspects of the system geometry remain fixed among experiments. Boundaries may be of infinite extent in simulations, or of finite extent in experiments, where the latter (i.e., specimen size) is fixed such that the domain size is not an independent variable.

It is also assumed that a system velocity, denoted by υ, is a defined, controllable constant for each simulation or experiment analyzed, and is not a dependent variable. For example, the system velocity υ can be simply assigned as the indenter velocity $\dot{h}$ if prescribed as a constant in a simulation,[14,36,73] or can be assigned as the initial (measured) projectile impact velocity for a spherical impact experiment.[55–58] In a dynamic hardness or dynamic indentation experiment using a SHPB, the indenter velocity is generally not constant, even during the loading phase[60,62]: a transient period may exist over which the indenter accelerates, and then the indenter always decelerates. In that case, the velocity of the striker bar could be used for υ as a measure of the input loading rate, or the average indenter velocity, if controlled, over some finite time interval of the loading phase could be used.[60]

4.1 Variable Identification

The analysis considers only global, scalar quantities that are either (1) imposed or extracted from indentation experiments or (2) homogeneous and stationary material properties. Local field variables (e.g., stress and strain distributions depending on position in the sample) are not addressed.

Application of concepts of dimensional analysis and Buckingham's Pi theorem begins with identification of all dependent and independent variables in dimensional form. Dependent variables are defined as follows:

- Indentation force P;
- Indentation contact radius a;
- Plastic work of indentation W^P:

$$W^P = \int_0^{h_r} P(h)\,\mathrm{d}h. \tag{24}$$

Note that quantification of W^P requires loading to a maximum depth h_m followed by unloading to a residual depth h_r at which $P = 0$. From these three dependent variables, other quantities of interest can be defined, for example:

- Mean pressure $\bar{p} = P/(\pi a^2)$ and constraint factor $c = \bar{p}/\sigma_0$;
- Average temperature rise in a volume $\bar{V}$ of material assuming adiabatic conditions: $\Delta\bar{T} = W^P/(\rho_0 c_V \bar{V})$, where the plastic zone volume can be estimated

as the cylindrical region $\bar{V} \approx \frac{3}{4}\pi^2 a^3$ as in other works.[5,17]

The inelastic constitutive model of Eq. 14 is assumed a priori, with $\zeta = 1$ in Eq. 17 for the adiabatic regime. As discussed in Section 3, linear isotropic elasticity is assumed without thermoelastic coupling, and as discussed in Section 4, frictionless contact is assumed. The material is also presumably homogeneous. In dimensional form, independent variables are then the following:

- Indentation depth h and maximum depth h_m;
- Effective indentation (system) velocity υ;
- Indenter radius R;
- Initial temperature T_0;
- Substrate elastic properties [dropping $(\cdot)_s$ subscripts] E, ν;
- Substrate plastic properties σ_0, κ, m, n, r, $\dot{\epsilon}_0$, T_R;
- Substrate initial mass density ρ_0 and specific heat per unit mass c_V.

Of these independent variables, only h varies with time during an indentation simulation or experiment, given the definition of υ as a constant explained already. The maximum depth is needed for determination of W^P, since h is multi-valued during a load-unload cycle.[7,12] However, h_m can be excluded from the list if only P and a are sought from a monotonic loading process. Sixteen independent variables are listed, of which 11 are material property constants. Time is not an explicit independent variable, since given the system velocity, indenter radius, initial temperature, and material properties, the time at which a particular depth value h is achieved is determined implicitly.[7]

Next, the Buckingham Pi theorem is invoked to reduce the number of independent variables when expressed in dimensionless form.[7,10,11,13] The number of independent dimensions entering the problem is four: mass, length, time, and temperature. Since the stress dimension is recovered from mass, length, and time, the four independent dimensions are reassigned into stress, length, time, and temperature. The following independent variable combinations are then used for normalization:

- Stress: modulus E;

- Length: indenter radius R;
- Time: viscoplastic time scale $t_0 = 1/\dot{\epsilon}_0$;
- Temperature: plastic thermal susceptibility $\tilde{T} = \sigma_0/(\rho_0 c_V)$.

The elastic modulus is a standard prescription for stress normalization.[7] Unlike analysis in prior works,[7,12,14,36] h and υ are herein excluded as normalization factors, since it is more convenient to work with constant quantities R and t_0, which later serve to define dimensionless strain and strain rate. Note that as t_0 decreases, plastic relaxation is faster and a rate-independent response is approached. Note also that as $\tilde{T}$ decreases, the tendency for adiabatic temperature rise decreases.

Applying the Pi theorem, the number of independent variables is reduced from 16 to 12, now defined in dimensionless form as

- Indentation depth h/R and maximum depth h_m/R;
- Indentation rate $(\upsilon/R) \cdot t_0$;
- Yield strength σ_0/E;
- Elastic wave speed via $R/(C_l t_0)$, where $C_l = \sqrt{E/\rho_0}$;
- Reference temperature $\tilde{T}/T_R$ and initial temperature $\tilde{T}/T_0$;
- Dimensionless elastic and plastic properties ν, κ, m, n, r.

The following physically appealing results are apparent. Normalized depth h/R is an approximate global strain measure. Normalized rate $\upsilon t_0/R$ is an approximate global measure of strain rate times plastic relaxation time, where the larger the value of this dimensionless quantity, the greater the viscoplastic rate effect. As $t_0 \to 0$ or $\upsilon \to 0$, the rate-independent case is recovered. Use of the ratio σ_0/E characterizes plastic to elastic stiffness, a standard choice.[7,14,36] The ratio $R/(C_l t_0)$ is interpreted as the elastic wave relaxation time R/C_l divided by viscoplastic relaxation time t_0. As $R/(C_l t_0) \to 0$, inertial effects should become less important since stress wave equilibrium should be achieved more rapidly relative to viscoplastic rate effects. Typically in practice, T_R is simply fixed at room temperature (≈ 294 K), but $\tilde{T}/T_R \to 0$ as the material becomes resistive to temperature change. Ambient temperature T_0 will differ from T_R for indentation at other thermal conditions (e.g., testing of pre-heated samples).

4.2 Functional Forms

Given the independent dimensionless variables, the sought dependent variables can be expressed as dimensionless functions Π_P, Π_a, Π_W:

$$\frac{P}{ER^2} = \Pi_P \left(\frac{h}{R}, \frac{\upsilon\, t_0}{R}, \frac{\tilde{T}}{T_0}; \frac{\sigma_0}{E}, \frac{R/t_0}{\sqrt{E/\rho_0}}, \frac{\tilde{T}}{T_R}, \nu, \kappa, m, n, r \right), \tag{25}$$

$$\frac{a}{R} = \Pi_a \left(\frac{h}{R}, \frac{\upsilon\, t_0}{R}, \frac{\tilde{T}}{T_0}; \frac{\sigma_0}{E}, \frac{R/t_0}{\sqrt{E/\rho_0}}, \frac{\tilde{T}}{T_R}, \nu, \kappa, m, n, r \right), \tag{26}$$

$$\frac{W^P}{ER^3} = \Pi_W \left(\frac{h}{R}, \frac{h_m}{R}, \frac{\upsilon\, t_0}{R}, \frac{\tilde{T}}{T_0}; \frac{\sigma_0}{E}, \frac{R/t_0}{\sqrt{E/\rho_0}}, \frac{\tilde{T}}{T_R}, \nu, \kappa, m, n, r \right). \tag{27}$$

Arguments preceding the the semicolons on the right sides of Eqs. 25–27 are loading conditions, and arguments following the semicolon are material properties. As noted in Section 4.1, h_m/R is not required for determination of force and contact area during monotonic loading so is excluded from Π_P and Π_a. Parametric experiments and/or FE simulations are needed to fully determine the functions on the right sides of Eqs. 25–27. Results from such studies will enable assessment of relative importance of loading rate, temperature, and material properties on the global mechanical and thermal response.

The isothermal, quasi-static Hertz solution should be recovered as $\sigma_0/E \to 0$, $\upsilon \to 0$, $\tilde{T} \to 0$, and $C_l \to \infty$, where for small indentation depths $R_s \to \infty$:

$$\Pi_P \left(\frac{h}{R}, 0, 0; 0, 0, 0, \nu, \kappa, m, n, r \right) = \frac{4}{3(1-\nu^2)} \left(\frac{h}{R} \right)^{3/2} \qquad [\bar{R} \to R], \tag{28}$$

$$\Pi_a \left(\frac{h}{R}, 0, 0; 0, 0, 0, \nu, \kappa, m, n, r \right) = \left(\frac{h}{R} \right)^{1/2} \qquad [\bar{R} \to R], \tag{29}$$

$$\Pi_W \left(\frac{h}{R}, \frac{h_m}{R}, 0, 0; 0, 0, 0, \nu, \kappa, m, n, r \right) = 0. \tag{30}$$

Analytical functional forms, if they can be determined, should be consistent with the limiting cases in Eqs. 28–30. Given Eqs. 25–27, the mean contact pressure, constraint factor, and temperature rise can be reconstructed:

$$\bar{p} = \frac{E}{\pi} \left(\frac{R}{a} \right)^2 \cdot \Pi_P \approx c\sigma_0, \qquad \Delta\bar{T} = \frac{4E}{3\pi^2} \left(\frac{R}{a} \right)^3 \cdot \Pi_W = \frac{4E}{3\pi^2} \cdot \frac{\Pi_W}{(\Pi_a)^3}. \tag{31}$$

Similarly, indentation strains[17,34] can be found as

$$\bar{\epsilon} = 0.2\frac{a}{R} = 0.2 \cdot \Pi_a, \qquad \hat{\epsilon} = \frac{4}{3\pi}\frac{h}{a} = \frac{4}{3\pi}\frac{h/R}{\Pi_a}. \tag{32}$$

If the constitutive model of Eq. 15 is used instead of Eq. 16, then the subset of two independent dimensionless variables (m, r) is replaced with the set of three dimensionless variables $(C, q, T_M/\tilde{T})$ in Eqs. 25–27.

5. Application to Instrumented Indentation Data

5.1 Experimental Protocols

Data from three dynamic spherical indentation experiments are analyzed using equations and techniques of Sections 2, 3, and 4. Experimental methods have been discussed by Casem[62] and summarized in what follows.

A miniature Kolsky bar (i.e., SHPB)[76] is adapted for instrumented indentation, whereby transient force, displacement, and velocity data are acquired in each experiment. The loading history (e.g., indenter velocity) depends on the velocity of the striker bar and geometric properties of the system (including pulse shaping) as well as indentation resistance afforded by the substrate. Initial clearance between indenter and substrate also affects the velocity history. The loading history is thus not strictly controlled; however, different final indentation depths are generally achieved by increasing the striker velocity, commensurate with an increase in the average loading rate. Experimental data include both the loading and unloading histories for each test.

Relevant properties and parameters are listed in Table 1 with supporting references. Of these values, the hardening, rate-, and temperature-sensitivity parameters $(\kappa, n, C, q, \dot{\epsilon}_0, T_M)$ are not used explicitly in the forthcoming analysis but are included for context to aid in interpretation of results. All current experiments are performed at standard room temperature: $T_0 = T_R$. Prominent results are summarized in Table 2 for reference, to be defined and discussed in detail later. Pertaining to loading conditions, h_m in the leftmost column is the maximum indentation depth prior to unloading, and $\dot{h}_A$ in the rightmost column is the average indenter tip velocity over the loading phase of each experiment.

Table 1 Material and geometric parameters

Parameter (units)	Value	Definition	Source
E (GPa)	71.0	modulus of Al 6061-T6	Wu et al.[77]
ν (-)	0.33	Poisson's ratio of Al 6061-T6	Wu et al.[77]
ρ_0 (g/cm^3)	2.77	mass density of Al 6061-T6	Wu et al.[77]
c_V (J/kg·K)	896	specific heat of Al 6061-T6	Zhu et al.[78]
σ_0 (GPa)	0.25	initial yield strength of Al 6061-T6	Lesuer et al.,[79] Zhu et al.[78]
κ (-)	0.35-1.8	hardening coefficient range of Al 6061-T6	Lesuer et al.,[79] Zhu et al.[78]
n (-)	0.38-0.43	hardening exponent range of Al 6061-T6	Lesuer et al.,[79] Zhu et al.[78]
$C \simeq m$ (-)	0.002-0.083	rate sensitivity range of Al 6061-T6	Lesuer et al.,[79] Zhu et al.,[78] Casem et al.[76]
$q \simeq -r$ (-)	1.34	thermal softening of Al 6061-T6	Lesuer et al.[79]
$\dot{\epsilon}_0$ (1/s)	1.0	reference strain rate (universal)	Zhu et al.[78]
T_M (K)	925	melt temperature of Al 6061-T6	Zhu et al.[78]
T_R (K)	294	reference temperature (ambient)	Zhu et al.[78]
$\bar{E}$ (GPa)	71.2	system modulus with WC indenter	Weaver et al.[1]
R (mm)	3.175	indenter radius	this work

Table 2 Loading conditions and results at max depth $(\cdot)_m$ or averaged results over the loading phase $(\cdot)_A$

Experiment	h_m (μm)	a_m (μm)	W_m^P (mJ)	$\Delta\bar{T}_m$ (K)	$\bar{\epsilon}_m$	$\hat{\epsilon}_m$	$\dot{\bar{\epsilon}}_A$ (1/s)	$\dot{\hat{\epsilon}}_A$ (1/s)	$\dot{h}_A$ (m/s)
1	17.2	421	1.57	1.15	0.0265	0.0174	1386	908	0.90
2	25.0	508	3.82	1.59	0.0320	0.0209	2217	1452	1.74
3	35.7	606	8.43	2.06	0.0382	0.0250	2750	1801	2.57

The indenter is tungsten carbide (WC) with a radius $R = R_i$ of 3.175 mm. The substrate is aluminum alloy Al6061-T6, of cylindrical geometry with $L_s/D_s = 1$ and $D_s = 4R_i = 4R$. Static spherical indentation experiments on this material have been reported elsewhere,[28] albeit with an indenter of larger radius $2R$. Numerical simulations of the static problem[28] loaded to comparable indentation strain levels suggest that the current dimensions of the substrate are sufficiently large to mitigate boundary edge effects. However, effects of stress wave interactions with finite boundaries cannot be ruled out in dynamic experiments.

The elastic stiffness of WC ($E_i = 640$ GPa) is an order of magnitude larger than that of aluminum, and $\bar{E}$ in Table 1 accounts for the correct modulus of both the indenter and substrate, assumed known a priori. If a rigid indenter is assumed instead, then $\bar{E}$ increases by $\approx 10\%$. However, since the indenter material is held fixed among experiments, elastic properties of the indenter can be excluded from the list of independent variables in the forthcoming dimensional analysis, as assumed in the general framework of Section 4.

The reported indentation depth and velocity account for far-field displacement (including rigid body motion) of the substrate but not the (presumably small) elastic deformation of the very stiff indenter tip. In the notation that follows, $h \approx h_s$ and $\dot{h} \approx \dot{h}_s$ are interpreted as the true indentation depth and depth rate in the substrate, relative to those measured for the far-field surface away from any pile-up or sink-in effects. Cursory calculations with the approximation in Eq. 3 confirm that the contribution of deformation of the indenter, h_i, to h should be negligible for loads and contact radii reported in what follows.

5.2 Data Analysis

Experimental force-depth, depth-time, and depth rate-time histories are shown in Fig. 1, labeled “exp” (experiment) 1, 2, and 3. The time t at a given depth h is confirmed by the integral $t = \int (h/\dot{h}) \mathrm{d}h$ where $\dot{h}$ is known as a function of h and initially $t = 0$. Shown for reference in Fig. 1a is the Hertz elastic solution of Eq. 1 obtained assuming $\bar{R} = R$.

For $h \gtrsim 10\,\mu$m, the data are more compliant than the elastic solution, as expected for an elastic-plastic material post yielding. For $h \lesssim 10\,\mu$m, experiments are similar to the elastic solution. Notably, some data appear slightly stiffer than the elastic

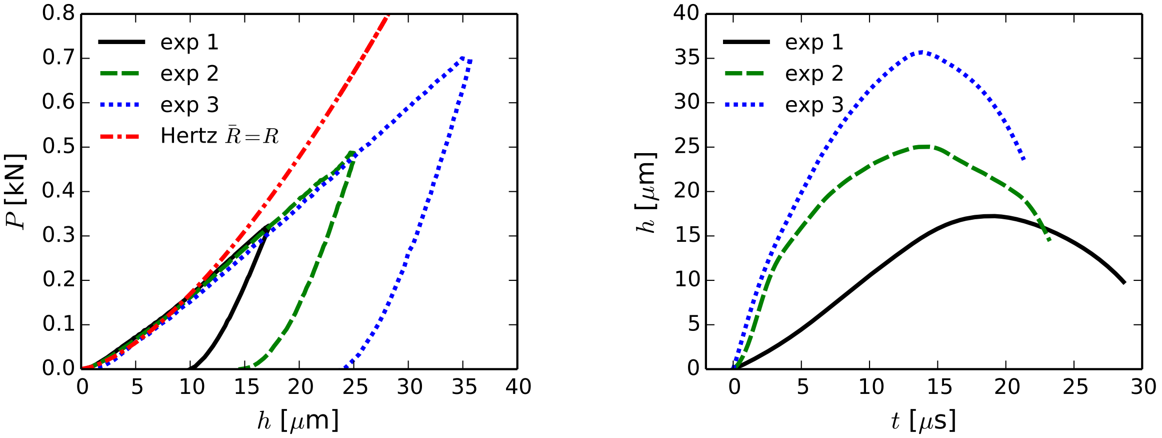

(a) force (b) depth

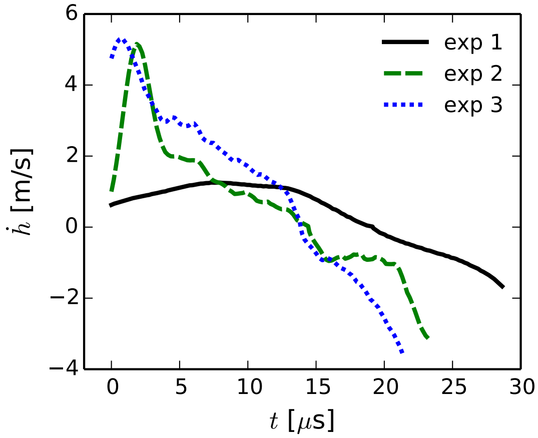

(c) velocity

Fig. 1 Experimental data: a) force vs depth with Hertz analytical solution, b) depth vs time, and c) depth rate vs time

solution over small intervals of h. These unusual features could be due to inertial effects and/or imprecision of experimental measurements at very low indentation depths. Depth-time histories shown in Fig. 1b indicate total load-unload durations ranging from around 20 to 30 μs. Maximum depth and depth rate increase with experiment number. Velocity histories are drastically different among experiments. For example, velocity ramps up quickly with time for experiment 2, while it is initially near maximal for experiment 3. In the latter case, the indenter clearly accelerates prior to contact with the substrate. Note $\dot{h} < 0$ during the unloading phase of each experiment. Peak loading and unloading velocities are notably smaller for experiment 1 than experiments 2 and 3.

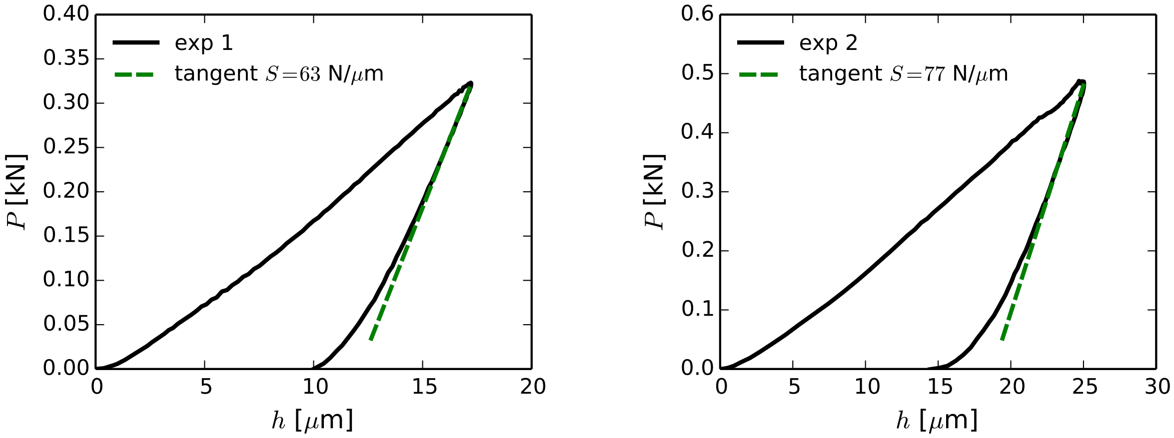

(a) experiment 1

(b) experiment 2

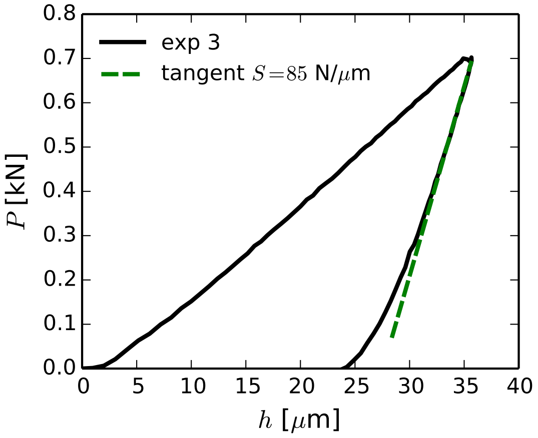

(c) experiment 3

Fig. 2 Data and unloading tangent: a) experiment 1, b) experiment 2, and c) experiment 3

Force-depth data are delineated for each experiment in Fig. 2, wherein the slope S upon initial unloading is extracted from the tangent for each case. The maximum indentation depth is denoted by h_m. The unloading slope S at $h = h_m$ is then used to obtain the Hertz contact radius at maximum depth $a_m = a(h = h_m)$, assuming quasi-static elastic unloading, via Eq. 5.[27,28] Elastic modulus $\bar{E}$ is assumed, a priori, to have the value listed in Table 1. No attempt is made to extract elastic properties from the present indentation data as has been done in some investigations elsewhere.[6]

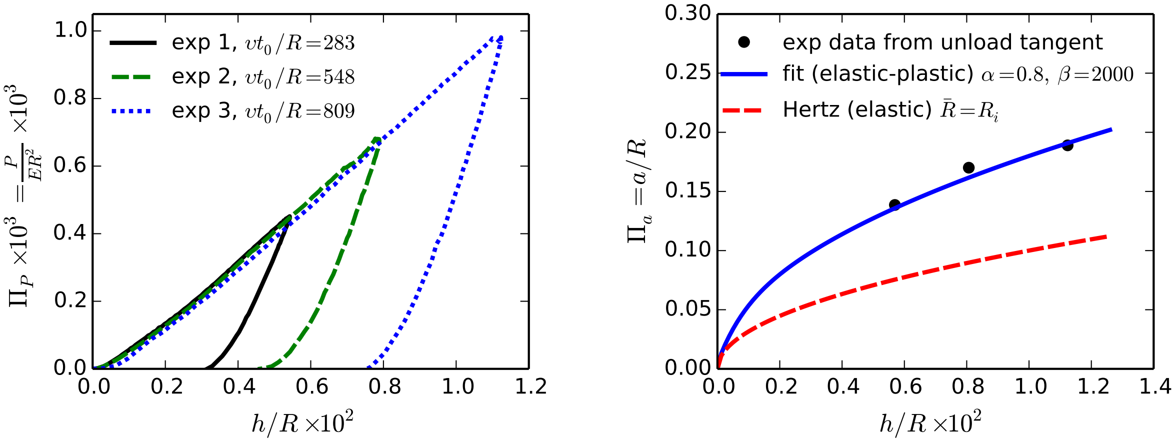

(a) force (b) contact radius

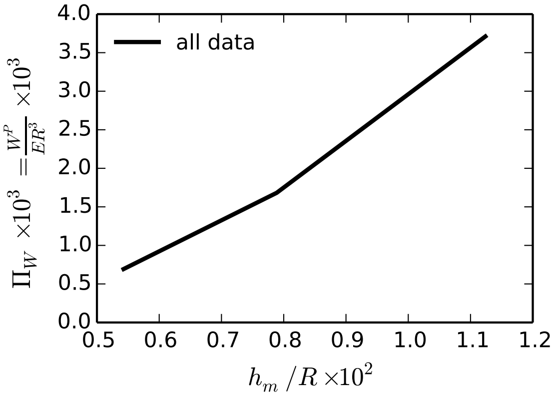

(c) plastic work

Fig. 3 Dimensionless variables: a) normalized force, b) contact radius, and c) plastic work

Dimensionless dependent variables (Π-terms) introduced in the analysis of Section 4 are reported in Fig. 3. General functional forms are Eqs. 25–27. In each figure, the independent variable resolved on the abscissa is dimensionless depth h/R (or h_m/R), which is well-defined and fully known from the data. Among different experiments, the normalized indentation velocity $\upsilon t_0/R$ also varies, as does the maximum normalized depth h_m/R. Since the substrate material and initial temperature (room temperature) are identical among experiments, the other independent variables on the right sides of Eqs. 25–27 are fixed among the present results. Hence, potential influences of the latter (fixed) properties cannot be discerned among the presently available data. A candidate definition for effective velocity is the average loading rate $\upsilon = \dot{h}_A = h_m/t_m$, where t_m is the time instant at which $h = h_m$. As shown in the rightmost column of Table 2, υ_A increases from 0.9 to 1.7 to 2.6 m/s over experiment numbers 1 to 2 to 3.

Normalized force Π_P versus normalized depth h/R in Fig. 3a provides the same information in Fig. 1a, since E and R are identical among experiments. Assuming $\upsilon = \dot{h}_A$, the results in Fig. 3a show that dependence of dimensionless indentation force Π_P on dimensionless loading rate $\upsilon t_0/R$ is low for Al-6061T6 over the current domain of loading rates.

Since the present data do not contain intermittent unload-reload cycles or continuous stiffness measurements (CSM) to obtain unloading slope $S(h)$ for $h \neq h_m$, approximations are used to compute contact radius $a(h)$ for $h \neq h_m$. First, for the loading phase, $t \leq t_m$, it is assumed that $a(t)$ for each experiment depends only on h/R and not υ. As shown in Fig. 3b, the normalized radius Π_a is then estimated by the following function, where $\alpha \geq 0$ and $\beta \gg 1$ are dimensionless fitting constants:

$$\Pi_a = a/R = (1 + \alpha\{1 - \exp(-\beta h/R)\})\sqrt{h/R} \qquad [t \leq t_m]. \tag{33}$$

The Hertz solution is recovered in the limit of infinitesimal depth, whereby $a \to \sqrt{hR}$.

Available data do not enable fitting of $a(t)$ for $t > t_m$, i.e., throughout the entire unloading process. Thus, during unloading, it is assumed that the indentation stress-strain data (specifically, $\bar{p}$ versus $\hat{\epsilon}$) demonstrate a fixed slope of $\bar{E}$, consistent with quasi-static unloading.[5,17] To this end, the following quadratic equation is solved at each time increment for $a(h(t))$ during the unloading phase:

$$\frac{4\bar{E}}{3\pi}\left(\frac{h}{a}-\frac{h_f}{a_f}\right)=\frac{P}{\pi a^2} \qquad [t \geq t_m]. \tag{34}$$

Here, h_f is the final (residual) indentation depth upon complete unloading, and a_f is the corresponding final contact radius. The latter can be computed by solving Eq. 34 at $h = h_m$ with corresponding peak load $P = P_m$ and radius $a = a_m$ from Eq. 33.

Finally, normalized plastic work Π_W is shown in Fig. 3c. Its computation requires the entire load-unload force-displacement cycle for a given h_m; hence, only three data points are available (one for each experiment). Though not shown in Fig. 3, Π_W logically could depend on h_f/R as well, since h_f varies among experiments, increasing from 9.8 to 14.4 to 23.6 μm over experiments 1, 2, and 3. Such dependency is permissible via inclusion of h/R in addition to h_m/R in the arguments of Eq. 27. However, the identity $\Pi_P(h = h_f) = 0$ provides an additional constraint equation that can be used to eliminate explicit dependence of Π_W on h_f/R. Normalized plastic work clearly increases with increasing maximum penetration depth.

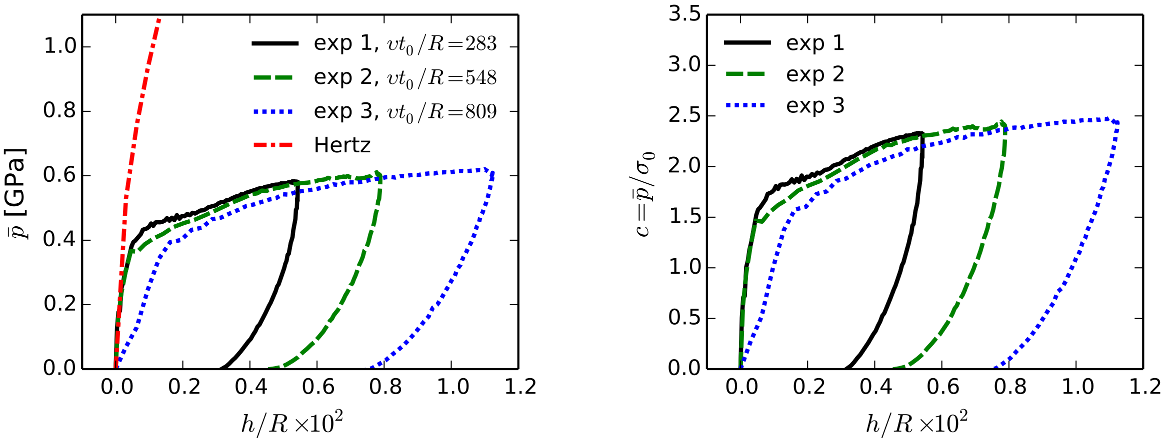

(a) mean pressure

(b) constraint factor

Fig. 4 Stress vs depth: a) mean pressure (hardness) and b) constraint factor

Given a (or equivalently, Π_a) along with force data $P(h)$, mean pressure $\bar{p} = P/(\pi a^2)$, i.e., Meyer's hardness, is computed. Results are shown in Fig. 4a. Constraint factor c is shown in Fig. 4b, where the initial yield stress σ_0 from Table 1 is used for normalization. Note that this value of σ_0 is considered to be known a priori, rather than extracted from the present indentation data. Mean pressure closely tracks the Hertz solution at a very small h/R for experiments 1 and 2, whereas $\bar{p}$ for experiment 3 suggests anomalously low compliance in the limit $h/R \rightarrow 0$. Mean pressures are similar among the loading phases of all three experiments for $h/R \gtrsim 0.0025$, in the regime where plastic compliance is expected to overtake elastic compliance. Such similarities suggest strain rate and strain rate–history effects on $\bar{p}$ are small for these experiments on Al6061-T6, given the very different velocity histories among tests in Fig. 1c.

Taking $v = \dot{h}_A$, the results in Fig. 4a suggest that dependence of mean stress on dimensionless loading rate vt_0/R is low. In fact, mean stress and constraint factor appear to decrease slightly with increasing loading rate, though such decrease may be due to imprecision of the experimental measurements and uncertainty inherent in Eq. 33 that neglects possible rate dependence of the transient contact radius.

Recall that initial yielding corresponds to $c \approx 1.1$ in the quasi-static Hertz theory.[6] After yielding, the calculated constraint factor increases from $c \approx 1.5$ to $c \approx 2.5$ over the full domain of indentation depths in the experiments. Strain hardening likely influences c to increase with increasing h/R in the fully plastic regime. The computed range of c is within bounds observed elsewhere in quasi-static spherical indentation experiments and simulations.[1,2,6,27,32–35] Similar ranges have been observed in dynamic spherical indentation simulations of elastic-perfectly plastic, rate-independent solids for constant rigid indenter velocities that are not too large (e.g., $\dot{h} \lesssim 75$ m/s), albeit for representative metallic substrates with different properties than those of aluminum.[36] Transient increases in c due to inertial effects manifest at velocities on the order of 100 m/s[36]; at such high velocities, effects of strain rate sensitivity on c also become stronger.[14] During elastic unloading, c is easily computed, but does not have any physical significance.

Indentation stress (i.e., mean pressure $\bar{p}$) is reported versus the two different indentation strain measures of Eq. 32 in Fig. 5. Elastic deformation followed by plastic yielding and mild to moderate strain hardening is apparent in each representation. The hardening behavior is qualitatively consistent with traditional dynamic uniaxial stress-strain behavior of this material.[76,78] The anomalously high initial compliance of experiment 3 is also apparent in Fig. 5. Elastic unloading is perfectly represented

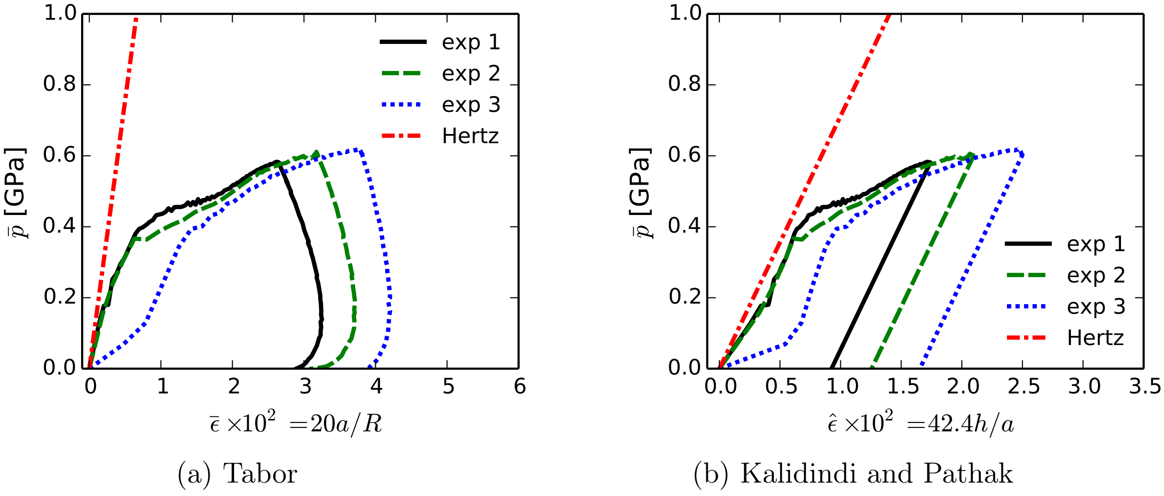

(a) Tabor

(b) Kalidindi and Pathak

Fig. 5 Indentation stress vs a) Tabor's strain[34] and b) Kalidindi and Pathak's strain[17]

in Fig. 5b as a result of implementation of Eq. 34. On the other hand, the unloading portions of $\bar{p}$ versus $\bar{\epsilon}$ curves in Fig. 5a show slopes inconsistent with $\bar{E}$. Similar inconsistencies have been noted when $\bar{\epsilon}$ is used as the indentation strain measure for static indentation.[5,17] In Fig. 5b, yielding is apparent at $\hat{\epsilon} \approx 0.6\%$ for experiments 1 and 2. From Eq. 13, with $c \approx 2.5$, the uniaxial equivalent yield strain is then estimated as $\sigma_0/E \approx 0.25\%$.

Strain rates in Eq. 19 and Eq. 22 are consistently obtained from numerical differentiation of Eq. 32. Results are shown in Fig. 6. According to each strain definition, strain rates are initially large where both the indentation depth and contact radius increase rapidly with time. Initial values of $\dot{\bar{\epsilon}}$ and $\dot{\hat{\epsilon}}$ range from 7,000/s to 28,000/s, with the highest strain rates observed in experiment 3. Strain rates decrease subsequently with increasing time, as the indenter necessarily decelerates. Negative rates persist during unloading. However, oscillations also arise during unloading to accommodate the assumed form of contact radius in the elastic response function of Eq. 34.

Due to uncertainty in assumed relations Eqs. 33 and 34, the strain rate histories shown in Fig. 6 should be considered highly approximate. However, average strain rates during the loading phase of each test should be much more accurate, since these do not rely on Eq. 33 or Eq. 34. Rather, such averages depend only on the

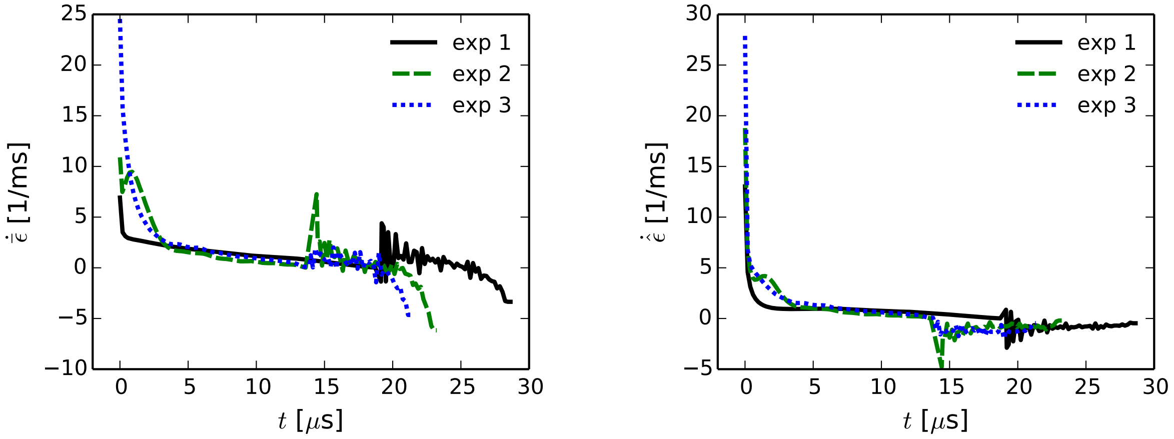

(a) Tabor (b) Kalidindi and Pathak

Fig. 6 Indentation strain rates from a) Tabor's strain[34] and b) Kalidindi and Pathak's strain[17]

unloading slope S in Eq. 5 used to obtain $a_m = \frac{1}{2}S/\bar{E}$ at known time t_m at the measured depth $h = h_m$:

$$\dot{\bar{\epsilon}}_A = 0.2\frac{a_m}{Rt_m}, \qquad \dot{\hat{\epsilon}}_A = \frac{4}{3\pi}\frac{h_m}{a_m t_m}. \tag{35}$$

Values of these average strain rates are listed in Table 2. Notably, average rates follow the same trends over all three experiments, with $\dot{\bar{\epsilon}}_A \approx 1.5\dot{\hat{\epsilon}}_A$ in each case. These average strain rates are within ranges that can be obtained in conventional uniaxial SHPB experiments.[78,79]

The same trends apply for maximum strains: $\bar{\epsilon}_m \approx 1.5\hat{\epsilon}_m$ in all three experiments. Values of $\hat{\epsilon}_m$ range from 1.8% to 2.5%. Taking $\hat{\beta} \approx 1.3$ in Eq. 13 as in earlier simulations of other elastic-plastic materials,[27] maximum uniaxial equivalent strains are then approximated as ranging from 1.4% to 1.9%.

Applying a representative rate sensitivity parameter of $C = 0.01$ from Table 1, the ratio of dynamic flow stress at a strain rate of 2000/s is only 7.6% higher than that at a rate of 1000/s. This result demonstrates the relatively low strain rate sensitivity of the Al6061-T6 material. Accordingly, any effects of different strain rates witnessed in experiments 1, 2, and 3 may be too small to be discerned in the load-displacement or indentation stress-strain curves. Such effects, if they exist, might also be obscured by limited fidelity of the data.

Other discrete data of interest are included in Table 2. Maximum depth h_m and corresponding contact radius a_m have been discussed already in the context of Fig. 3a and Fig. 3b. Average velocities $\dot{h}_A$ have been used to represent υ entering dimensionless rates in the legends of Fig. 3a and Fig. 4a. Likewise, plastic work W^P_m has been used in construction of Fig. 3c. Note that W^P_m is the residual plastic work after complete unloading from depth h_m.

Average adiabatic temperature rise ΔT_m is computed from Eq. 31, with $W^P = W^P_m$ and $a = a_m$. This is the temperature change that would be experienced by a cylindrical column of plastically deformed material of radius a_m and height $\frac{3}{4}\pi a_m$.[5,17] Given the temperature sensitivity $q \approx 1$ of Al6061-T6 in Table 1, the predicted heating-induced change in flow stress for this volume of material would be negligible. However, localized temperature increases in regions of concentrated plastic strain (e.g., near the edges of the contact surface) could be substantially larger, whereas heat conduction could counteract such increases given sufficient time. Thus, thermal effects cannot be completely ruled out without verification from simulations, for example.

5.3 Recommendations

The following key points are noted from analysis of the dynamic indentation data:

- Maximum uniaxial-equivalent strains are estimated on the order of 1% to 2%;
- Average uniaxial-equivalent strain rates are estimated on the order of 700 to 1500/s;
- Subtle variations in indentation force-depth curves can lead to drastic changes in indentation stress-strain curves, particularly at small indentation depths;
- Dynamic indentation stress-strain curves are qualitatively similar to those given elsewhere[27,28] for static spherical indentation, with constraint factors within ranges observed for static experiments on ductile metals;
- Mean pressure (i.e., indentation stress) shows evidence of yielding and mild-to-moderate strain hardening characteristic in uniaxial stress-strain data for the aluminum alloy;
- Strain rate and inertial effects are not detected among the experimental datasets,

whereby an increase in average indentation strain rate by a factor of 2 produces no apparent increase in indentation stress;

- A negligible effect of average strain rate correlates with the low strain rate sensitivity of flow stress for the aluminum alloy;
- Plastic work results in a trivially small adiabatic temperature rise ($\lesssim$ 2K) averaged over the entire plastically deformed zone, though magnitudes of localized temperature increases at plastic strain concentrations are unknown.

Consider the inverse problem of determination of material parameters from recorded dimensionless indentation force versus normalized depth, i.e., Π_P versus h/R data. In dynamic experiments, dimensionless response function Π_a for contact radius cannot be measured at present over the deformation history, and dimensionless response function Π_W ultimately offers no additional information over Π_P since the former can be constructed from the history of the latter.

The inverse problem can be stated as follows:

- Given $\frac{P}{ER^2} = \Pi_P \left(\frac{h}{R}, \frac{\upsilon\, t_0}{R}, \frac{\tilde{T}}{T_0}; \frac{\sigma_0}{E}, \frac{R/t_0}{\sqrt{E/\rho_0}}, \frac{\tilde{T}}{T_R}, \nu, \kappa, m, n, r \right)$ versus $\frac{h}{R}$ for different effective loading rates $\frac{\upsilon t_0}{R}$ and initial temperatures $\frac{\tilde{T}}{T_0}$, determine the 11 material properties $E, \nu, \rho_0, c_V, \sigma_0, \kappa, \dot{\epsilon}_0 = t_0^{-1}, m, n, r, T_R$.

Based on dimensional analysis of available results, the following deductions and recommendations are then proposed to facilitate the solution of the inverse problem:

- The relatively small magnitudes of impact velocities and the similarities of static and dynamic indentation curves suggest that inertial effects associated with ρ_0 cannot be discerned in the data. Thus, a standard (e.g., Archimedes) method should be used to measure ρ_0.
- The relatively low changes in average temperature suggest that effects of specific heat capacity c_V cannot be easily discerned in the force response data. Thus, a standard (e.g., calorimetry) method should be used to measure c_V.
- Precision of current experimental methods in the very small-depth regime is likely insufficient to measure elastic compliance. Thus, a standard (e.g., longitudinal and shear wave speed) method should be used to measure E and

ν. Any experimental facility equipped for dynamic instrumented indentation should include the capability for such sound speed measurements, presuming material samples are available.

- Precision of current experimental methods is likely inadequate for determination of an "exact" initial yield stress σ_0. However, an offset yield stress should be measurable, which can provide an approximate value of σ_0 as in static experiments.[27]
- For low loading rates or rate-insensitive materials, extraction of static hardening parameters κ and n should be possible from measured increases of Π_P with increasing h/R.
- Effects of loading rate vt_0/R on Π_P for highly rate-sensitive materials remains unknown. Experiments on other solids with much greater strain rate sensitivity of flow stress are needed to determine if such rate sensitivity manifests in dynamic indentation force-displacement (and corresponding indentation stress-strain) curves. If differences in Π_P at vastly different vt_0/R do not manifest for such materials, the present experimental method might be unsuitable to extract rate sensitivity parameters (e.g., m, or C if Eq. 15 is used).
- Following typical protocols,[66,78] the two parameters $\dot{\epsilon}_0$ and T_R can be set universally at 1/s and 294 K, which reduces complexity of the inverse problem.
- Presumably, systematic matching of experimental Π_P data with results of parametric FE simulations on the same geometry (sample size and R), loading rate, and initial temperature, and covering a sufficient domain of possible material property sets, will produce the sought material properties. Similar efforts have been undertaken for static indentation as reviewed in Section 2.3, though most not often invoking dimensional analysis techniques.
- Existence, uniqueness, stability, and accuracy of the inverse method should be verified for multiple materials, with constitutive properties validated by comparison with values obtained from independent, alternative experimental techniques (e.g., standard SHPB compression tests rather than dynamic indentation).

Several other recommendations are in order. Firstly, experimental methods to directly measure the contact radius during dynamic indentation could supply data that would render the assumed rate-independent forms in Eqs. 33 and 34 unnecessary. Efforts are presently underway to measure residual impressions with confocal microscopy. Techniques involving periodic dynamic unloading in the SHPB apparatus to measure contact stiffness are under development,[62] though their accuracy remains unclear.

While knowledge of $a = \Pi_A \cdot R$ is not needed to solve the stated inverse problem, the contact radius is needed to calculate indentation stress (mean pressure) $\bar{p}$ as well as indentation strains $\bar{\epsilon}$ and $\hat{\epsilon}$. Constitutive property extraction might be more efficient and accurate by matching experimental and simulated indentation stress-strain curves rather than matching Π_P vs. h/R.

Comparison of static and dynamic isothermal FE simulations on the same geometry (i.e., same sample size and R), for a hypothetical rate-independent material, would enable verification of the tentative conclusion that inertial effects are negligible for the present range of loading rates. Lastly, adiabatic FE simulations could be used to provide an upper bound on localized temperature rise in highly strained regions under the indenter, and thus verify the tentative conclusion that effects of temperature rise (but not necessarily initial temperature) on indentation force are negligible over the present range of loading rates.

6. Conclusions

Analytical foundations for interpretation of data from instrumented dynamic spherical indentation experiments have been established in this work. The ultimate intent is acquiring constitutive properties, here focused on plastic properties of ductile metals, from dynamic indentation force-depth data at different loading rates and different initial temperatures. A new framework to guide future experiments and numerical simulations has been set forth based on principles of dimensional analysis. Potential utility, and limitations, of the framework have been assessed using new data on Al6061-T6 obtained from SHPB experiments equipped for instrumented spherical indentation. Average strain rates achieved in experiments are on the order of 10^3/s, with maximum equivalent strains on the order of 2%. Indentation stress-strain results verify that rate sensitivity of the alloy is low.

7. References

1. Weaver J, Khosravani A, Castillo A, Kalidindi S. High throughput exploration of process-property linkages in Al-6061 using instrumented spherical microindentation and microstructurally graded samples. Integrating Materials and Manufacturing Innovation. 2016;5:192–211.

2. Taljat B, Zacharia T, Kosel F. New analytical procedure to determine stress-strain curve from spherical indentation data. International Journal of Solids and Structures. 1998;35:4411–4426.

3. Mesarovic S, Fleck N. Spherical indentation of elastic–plastic solids. Proceedings of the Royal Society of London A. 1999;455:2707–2728.

4. Clayton J. Spherical indentation in elastoplastic materials: modeling and simulation. US Army Research Laboratory; 2005. Report No.: ARL-TR-3516.

5. Pathak S, Kalidindi S. Spherical nanoindentation stress–strain curves. Materials Science and Engineering R. 2015;91:1–36.

6. Field J, Swain M. A simple predictive model for spherical indentation. Journal of Materials Research. 1993;8:297–306.

7. Cheng YT, Cheng CM. Scaling, dimensional analysis, and indentation measurements. Materials Science and Engineering R. 2004;44:91–149.

8. Barick M, Gaillard Y, Lejeune A, Amiot F, Richard F. On the uniqueness of intrinsic viscoelastic properties of materials extracted from nanoindentation using FEMU. International Journal of Solids and Structures. 2020;202:929–946.

9. Chen X, Hutchinson J, Evans A. The mechanics of indentation induced lateral cracking. Journal of the American Ceramic Society. 2005;88:1233–1238.

10. Buckingham E. On physically similar systems; illustrations of the use of dimensional equations. Physical Review. 1914;4:345–376.

11. Sedov L. Similarity and dimensional methods in mechanics. Academic Press; 1959.

12. Ni W, Cheng YT, Cheng CM, Grummon D. An energy-based method for analyzing instrumented spherical indentation experiments. Journal of Materials Research. 2004;19:149–157.

13. Clayton J. Penetration resistance of armor ceramics: dimensional analysis and property correlations. International Journal of Impact Engineering. 2015;85:124–131.

14. Lee A, Komvopoulos K. Dynamic spherical indentation of strain hardening materials with and without strain rate dependent deformation behavior. Mechanics of Materials. 2019;133:128–137.

15. Johnson K. Contact mechanics. Cambridge University Press; 1985.

16. Ghaednia H, Wang X, Saha S, Xu Y, Sharma A, Jackson R. A review of elastic–plastic contact mechanics. Applied Mechanics Reviews. 2017;69:060804.

17. Kalidindi S, Pathak S. Determination of the effective zero-point and the extraction of spherical nanoindentation stress–strain curves. Acta Materialia. 2008;56:3523–3532.

18. Clayton J, Becker R. Modeling nonlinear elastic-plastic behavior of RDX single crystals during indentation. US Army Research Laboratory; 2005. Report No.: ARL-TR-5864.

19. Dao M, Chollacoop N, Van Vliet K, Venkatesh T, Suresh S. Computational modeling of the forward and reverse problems in instrumented sharp indentation. Acta Materialia. 2001;49:3899–3918.

20. Chollacoop N, Dao M, Suresh S. Depth-sensing instrumented indentation with dual sharp indenters. Acta Materialia. 2003;51:3713–3729.

21. Cao YP, Lu J. A new method to extract the plastic properties of metal materials from an instrumented spherical indentation loading curve. Acta Materialia. 2004;52:4023–4032.

22. Johnson K. The correlation of indentation experiments. Journal of the Mechanics and Physics of Solids. 1970;18:115–126.

23. Zhao M, Ogasawara N, Chiba N, Chen X. A new approach to measure the elastic–plastic properties of bulk materials using spherical indentation. Acta Materialia. 2006;54:23–32.

24. Phadikar J, Bogetti T, Karlsson A. Aspects of experimental errors and data reduction schemes from spherical indentation of isotropic materials. Journal of Engineering Materials and Technology. 2014;136:031005.

25. Le MQ. Material characterization by instrumented spherical indentation. Mechanics of Materials. 2012;46:42–56.

26. Donohue B, Ambrus A, Kalidindi S. Critical evaluation of the indentation data analyses methods for the extraction of isotropic uniaxial mechanical properties using finite element models. Acta Materialia. 2012;60:3943–3952.

27. Patel D, Kalidindi S. Correlation of spherical nanoindentation stress-strain curves to simple compression stress-strain curves for elastic-plastic isotropic materials using finite element models. Acta Materialia. 2016;112:295–302.

28. Fernandez-Zelaia P, Joseph V, Kalidindi S, Melkote S. Estimating mechanical properties from spherical indentation using bayesian approaches. Materials & Design. 2018;147:92–105.

29. Lu L, Dao M, Kumar P, Ramamurty U, Karniadakis G, Suresh S. Extraction of mechanical properties of materials through deep learning from instrumented indentation. Proceedings of the National Academy of Sciences. 2020;117:7052–7062.

30. Chen G, Zhang X, Zhong J, Shi J, Wang Q, Guan K. New inverse method for determining uniaxial flow properties by spherical indentation test. Chinese Journal of Mechanical Engineering. 2021;34:94.

31. Simo J, Hughes T. Computational inelasticity. Springer-Verlag; 1998.

32. Francis H. Phenomenological analysis of plastic spherical indentation. Journal of Engineering Materials and Technology. 1976;98:272–281.

33. Matthews J. Indentation hardness and hot pressing. Acta Metallurgica. 1980;28:311–318.

34. Tabor D. The hardness of metals. Oxford University Press; 1951.

35. Hill R, Storåkers B, Zdunek A. A theoretical study of the Brinell hardness test. Proceedings of the Royal Society of London A. 1989;423:301–330.

36. Lee A, Komvopoulos K. Dynamic spherical indentation of elastic-plastic solids. International Journal of Solids and Structures. 2018;146:180–191.

37. Follansbee P, Sinclair G. Quasi-static normal indentation of an elasto-plastic half-space by a rigid sphere–I: Analysis. International Journal of Solids and Structures. 1984;20:81–91.

38. Bhattacharya A, Nix W. Finite element simulation of indentation experiments. International Journal of Solids and Structures. 1988;24:881–891.

39. Lee H, Lee JH, Pharr G. A numerical approach to spherical indentation techniques for material property evaluation. Journal of the Mechanics and Physics of Solids. 2005;53:2037–2069.

40. Moussa C, Hernot X, Bartier O, Delattre G, Mauvoisin G. Identification of the hardening law of materials with spherical indentation using the average representative strain for several penetration depths. Materials Science and Engineering A. 2014;606:409–416.

41. Moussa C, Hernot X, Bartier O, Delattre G, Mauvoisin G. Evaluation of the tensile properties of a material through spherical indentation: definition of an average representative strain and a confidence domain. Journal of Materials Science. 2014;49:592–603.

42. Arizzi F, Rizzi E. Elastoplastic parameter identification by simulation of static and dynamic indentation tests. Modelling and Simulation in Materials Science and Engineering. 2014;22:035017.

43. Dean J, Clyne T. Extraction of plasticity parameters from a single test using a spherical indenter and FEM modelling. Mechanics of Materials. 2017;105:112–122.

44. Huber N, Tsakmakis C. Determination of constitutive properties from spherical indentation data using neural networks. Part I: the case of pure kinematic hardening in plasticity laws. Journal of the Mechanics and Physics of Solids. 1999;47:1569–1588.

45. Huber N, Tsakmakis C. Determination of constitutive properties from spherical indentation data using neural networks. Part II: plasticity with nonlinear isotropic and kinematic hardening. Journal of the Mechanics and Physics of Solids. 1999;47:1589–1607.

46. Wang M, Wang W. An inverse method for measuring elastoplastic properties of metallic materials using Bayesian model and residual imprint from spherical indentation. Materials. 2021;14:7105.

47. Clayton J, Becker R. Elastic-plastic behavior of cyclotrimethylene trinitramine single crystals under spherical indentation: modeling and simulation. Journal of Applied Physics. 2012;111:063512.

48. Patel D, Al-Harbi H, Kalidindi S. Extracting single-crystal elastic constants from polycrystalline samples using spherical nanoindentation and orientation measurements. Acta Materialia. 2014;79:108–116.

49. Cheng YT, Cheng CM. Relationships between hardness, elastic modulus, and the work of indentation. Applied Physics Letters. 1998;73:614–616.

50. Cheng YT, Li Z, Cheng CM. Scaling relationships for indentation measurements. Philosophical Magazine A. 2002;82:1821–1829.

51. Chen X, Ogasawara N, Zhao M, Chiba N. On the uniqueness of measuring elastoplastic properties from indentation: the indistinguishable mystical materials. Journal of the Mechanics and Physics of Solids. 2007;55:1618–1660.

52. Liu L, Ogasawara N, Chiba N, Chen X. Can indentation technique measure unique elastoplastic properties. Journal of Materials Research. 2009;24:784–800.

53. Cao Y, Lu J. Depth-sensing instrumented indentation with dual sharp indenters: stability analysis and corresponding regularization schemes. Acta Materialia. 2004;52:1143–1153.

54. Barick M. Identification of the viscoelastic-viscoplastic properties of materials by instrumented nanoindentation [thesis]. Université Bourgogne Franche-Comté; 2020.

55. Mok CH, Duffy J. The dynamic stress-strain relation of metals as determined from impact tests with a hard ball. International Journal of Mechanical Sciences. 1965;7:355–371.

56. Tirupataiah Y, Sundararajan G. A dynamic indentation technique for the characterization of the high strain rate plastic flow behaviour of ductile metals and alloys. Journal of the Mechanics and Physics of Solids. 1991;39:243–271.

57. Sundararajan G, Tirupataiah Y. The localization of plastic flow under dynamic indentation conditions: I. Experimental results. Acta Materialia. 2006;54:565–575.

58. Sundararajan G, Tirupataiah Y. The localization of plastic flow under dynamic indentation conditions: II. Analysis of results. Acta Materialia. 2006;54:577–586.

59. Anton R, Subhash G. Dynamic Vickers indentation of brittle materials. Wear. 2000;239:27–35.

60. Subhash G. Dynamic indentation testing. ASM Handbook on Mechanical Testing and Evaluation. 2000;8:519–529.

61. Li S, Haozhe L. A new technique of dynamic spherical indentation based on SHPB. In: Dynamic Behavior of Materials; Vol. 1. Song B, Casem D, Kimberley J, editors. Springer; 2014. p. 81–87.

62. Casem D. A model for a Kolsky bar experiment: application to experiment design. DEVCOM Army Research Laboratory; 2022. Report No.: ARL-TR-9416.

63. Lu J, Suresh S, Ravichandran G. Dynamic indentation for determining the strain rate sensitivity of metals. Journal of the Mechanics and Physics of Solids. 2003;51:1923–1938.

64. Calle M, Mazzariol L, Alves M. Strain rate sensitivity assessment of metallic materials by mechanical indentation tests. Materials Science and Engineering A. 2018;725:274–282.

65. Mallick D, Zhao M, Parker J, Kannan V, Bosworth B, Sagapuram D, Foster M, Ramesh K. Laser-driven flyers and nanosecond-resolved velocimetry for spall studies in thin metal foils. Experimental Mechanics. 2019;59:611–628.

66. Johnson G, Cook W. A constitutive model and data for materials subjected to large strains, high strain rates, and high temperatures. In: Proceedings of the 7th International Symposium on Ballistics; p. 541–547.

67. Ito K, Arai M. Expanding cavity model combined with Johnson-Cook constitutive equation for the dynamic indentation problem. Journal of Engineering Materials and Technology. 2020;142:021005.

68. Clayton J, Lloyd J. A dynamic finite-deformation constitutive model for steels undergoing slip, twinning, and phase changes. Journal of Dynamic Behavior of Materials. 2021;7:217–247.

69. Clayton J. Nonlinear mechanics of crystals. Springer; 2011.

70. Kren A, Rudnitskii V, Lantsman G, Khudoley A. Influence of the dynamic indentation parameters on the behavior of metals during the penetration of an indenter with a spherical tip. Russian Metallurgy. 2021;2021:563–569.

71. Kumaraswamy A, Rao V. High strain-rate plastic flow behavior of Ti-6Al-4V from dynamic indentation experiments. Materials Science and Engineering A. 2011;528:1238–1241.

72. Ito K, Arai M. Simple estimation method for strain rate sensitivity based on the difference between the indentation sizes formed by spherical-shaped impactors. International Journal of Mechanical Sciences. 2021;189:106007.

73. Si B, Li Z, Xiao G, Shu X. Determination of mechanical properties from sharp dynamic indentation. Journal of Strain Analysis for Engineering Design. 2021;in press.

74. Kashfi M, Goodarzi S, Rastgou M. Plastic properties determination using virtual dynamic spherical indentation test and machine learning algorithms. Journal of Mechanical Science and Technology. 2022;36:325–331.

75. Atkins A, Tabor D. Plastic indentation in metals with cones. Journal of the Mechanics and Physics of Solids. 1965;13:149–164.

76. Casem D, Grunschel S, Schuster B. Normal and transverse displacement interferometers applied to small diameter Kolsky bars. Experimental Mechanics. 2012;52:173–184.

77. Wu B, Cao Y, Zhao J, Ding W. The effect of superimposed ultrasonic vibration on tensile behavior of 6061-T6 aluminum alloy. International Journal of Advanced Manufacturing Technology. 2021;116:1843–1854.

78. Zhu D, Mobasher B, Rajan S, Peralta P. Characterization of dynamic tensile testing using aluminum alloy 6061-T6 at intermediate strain rates. ASCE Journal of Engineering Mechanics. 2011;137:669–679.

79. Lesuer D, Kay G, LeBlanc M. Modeling large-strain, high-rate deformation in metals. Lawrence Livermore National Laboratory; 2001. Report No.: UCRL-JC-134118.

List of Symbols, Abbreviations, and Acronyms

TERMS:

Al	aluminum
ARL	Army Research Laboratory
CSM	continuous stiffness measurement
DEVCOM	US Army Combat Capabilities Development Command
FE	finite element
SHPB	split Hopkinson pressure bar
WC	tungsten carbide

MATHEMATICAL SYMBOLS:

E	modulus
h	depth
p	pressure
P	force
t	time
W	work
ϵ	strain
σ	stress
υ	velocity

1 DEFENSE TECHNICAL
(PDF) INFORMATION CTR
DTIC OCA

1 DEVCOM ARL
(PDF) FCDD RLD DCI
TECH LIB

1 CALIFORNIA INST TECH
(PDF) K BHATTACHARYA

1 GEORGIA INST TECH
(PDF) S KALIDINDI

1 IOWA STATE UNIV
(PDF) S PATHAK

2 JOHNS HOPKINS UNIV
(PDF) L GRAHAM-BRADY
K RAMESH

1 US NAVAL ACADEMY
(PDF) E RETZLAFF

26 DEVCOM ARL
(PDF) FCDD RLC HC
J CRONE
J KNAP
FCDD RLD FR
M TSCHOPP
FCDD RLW
J CIEZAK
S SCHOENFELD
FCDD RLW B
R BECKER
A TONGE
FCDD RLW MB
J LIGDA
Z WILSON
FCDD RLW ME
J SWAB
L VARGAS-GONZALEZ
FCDD RLW MF
C HAINES
FCDD RLW T
M FERMEN-COKER
R FRANCART
FCDD RLW TB
D CASEM
J CLAYTON
P MCKEE
C MEREDITH
R REGUEIRO
S SATAPATHY
FCDD RLW TE
J LLOYD
T SCHARF
FCDD RLW TF
J CAZAMIAS
P JANNOTTI
R LEAVY
D MALLICK